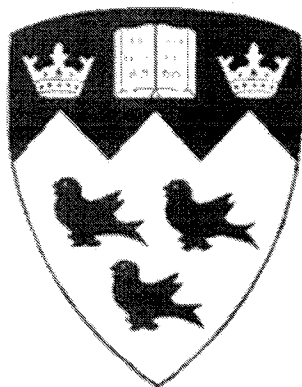


Simulation of Antenna Properties and Behaviour in Lossy Dispersive Media of the Human Tissues

Yi Zhang



Department of Electrical & Computer Engineering
McGill University
Montreal, Canada

April 2007

A thesis submitted to McGill University in partial fulfillment of the
requirements for the degree of Master of Engineering

© Yi Zhang 2007



Library and
Archives Canada

Published Heritage
Branch

395 Wellington Street
Ottawa ON K1A 0N4
Canada

Bibliothèque et
Archives Canada

Direction du
Patrimoine de l'édition

395, rue Wellington
Ottawa ON K1A 0N4
Canada

Your file *Votre référence*
ISBN: 978-0-494-38499-2
Our file *Notre référence*
ISBN: 978-0-494-38499-2

NOTICE:

The author has granted a non-exclusive license allowing Library and Archives Canada to reproduce, publish, archive, preserve, conserve, communicate to the public by telecommunication or on the Internet, loan, distribute and sell theses worldwide, for commercial or non-commercial purposes, in microform, paper, electronic and/or any other formats.

The author retains copyright ownership and moral rights in this thesis. Neither the thesis nor substantial extracts from it may be printed or otherwise reproduced without the author's permission.

AVIS:

L'auteur a accordé une licence non exclusive permettant à la Bibliothèque et Archives Canada de reproduire, publier, archiver, sauvegarder, conserver, transmettre au public par télécommunication ou par l'Internet, prêter, distribuer et vendre des thèses partout dans le monde, à des fins commerciales ou autres, sur support microforme, papier, électronique et/ou autres formats.

L'auteur conserve la propriété du droit d'auteur et des droits moraux qui protègent cette thèse. Ni la thèse ni des extraits substantiels de celle-ci ne doivent être imprimés ou autrement reproduits sans son autorisation.

In compliance with the Canadian Privacy Act some supporting forms may have been removed from this thesis.

While these forms may be included in the document page count, their removal does not represent any loss of content from the thesis.

Conformément à la loi canadienne sur la protection de la vie privée, quelques formulaires secondaires ont été enlevés de cette thèse.

Bien que ces formulaires aient inclus dans la pagination, il n'y aura aucun contenu manquant.


Canada

Abstract

The work reported in this thesis is motivated by the need for wireless powering of a miniaturized implantable device for neurophysiological research and possible clinical applications. The antenna used in such applications must be studied in the context of biological tissue media. In this thesis, we perform a preliminary study of antenna behaviour in the complex tissue environment. Our test cases are the wire dipole antenna chosen for its structural simplicity and the spiral antenna, selected for its wide bandwidth. The simulation tool SEMCAD-X, is based on the Finite-Difference Time-Domain (FDTD) method and is used throughout this work. To have an in-depth understanding of the characteristics of different solvers implemented in SEMCAD-X and relevant for our applications, we first simulate the antenna structures in the free-space region using both SEMCAD-X and HFSS (a Finite-Element Method (FEM) simulation software). The cross-platform comparison between these two simulation tools helps us identify the advantages of using conformal FDTD solver over the conventional staircase FDTD solver in SEMCAD-X. We then embed the antennas in tissue-like non-homogeneous lossy media to observe the terminal voltages induced by an impinging plane-wave. These numerical experiments will help us with the assessment of the following: variations of antenna properties with the in-tissue locations, and more importantly the dependence of the induced voltage on the depth of the implant.

Sommaire

Cette thèse présente un travail motivé par le besoin de “fournir de l’énergie sans fil à un appareil miniaturisé implantable” pour la recherche neurophysiologique et pour des applications cliniques. L’antenne utilisée dans telles applications doit être étudié quant au tissu biologique. Dans cette thèse, nous réalisons une étude préliminaire du comportement d’antenne en ce qui concerne le domaine complexe de tissu. Nous avons étudié l’antenne dipôle, choisi pour sa simplicité (structurelle), et l’antenne spirale, choisi pour sa largeur de bande. SEMCAD-X, un instrument de simulation, est fondé sur la méthode de “Finite-Difference Time-Domain” et cette méthode est utilisée pendant le cours de ce travail. Pour comprendre plus profondément les différentes caractéristiques des résolutions que SEMCAD-X applique et celles qui sont pertinentes à nos applications, nous commençons par simuler les antennes utilisant SEMCAD-X aussi bien qu’HFSS (fondé sur la méthode de « Finite Elements »). La comparaison des deux outils de simulation nous permet d’identifier les avantages d’utiliser la résolution FDTD conforme au lieu de la résolution « staircase » FDTD conventionnel utilisé par SEMCAD-X. De plus, nous avons enfoncé les antennes dans un médium « lossy » non homogène répliquant du tissu, en effet pour observer la tension au terminal causé par « impinging plane-wave ». Ces expériences numériques nous aideront avec l’évaluation de ce qui suit: les variations des propriétés d’antenne en fonction de son endroit dans le tissu, et plus important encore, la dépendance de tension induite avec la profondeur de l’implant.

Acknowledgements

I am grateful to my supervisor, Dr. Milica Popović for her kind support and patience during my work.

I would like to thank Mr. Houssam Kanj and Guanran (Kevin) Zhu in the CAD lab. They always generously shared with me their knowledge and their most interesting ideas. I also like to thank Ms Zahra Al-Roubaie for her help in translating the abstract into French.

I would also like to thank my parents and my grandparents who have given me nothing but their endless love and support. I wish my grandmother who past away while I was preparing this thesis rests in her peace.

I wish to thank my wife, Yingying Sun, who has always understood and supported me. Her constant encouragement and valuable advice have given me motivation to work hard.

The staff of Schmid and Partner Engineering AG provided and assisted us with SEMCAD-X software. We appreciate their help.

This work was supported in part by Natural Sciences and Engineering Research Council (NSERC) of Canada.

Table of Contents

1. Introduction.....	1
2. Background Review.....	2
2.1) RF Bio-Telemetry and Antenna Behaviour.....	2
2.1.1 RF Bio-Telemetry.....	2
2.1.2 Numerical Analysis of Embedded Antenna in Biological Tissue.....	5
2.1.2.1 Spherical Dyadic Green's Functions (DGF)	5
2.1.2.2 Finite-Difference Time Domain (FDTD Method)	8
2.1.2.3 Sample Studies of Antenna Behaviour in Embedded Environment..	11
2.2) Parameters of Tissue Layers.....	12
2.2.1 Thickness of Tissue Layers.....	13
2.2.2 Relative Permittivity and Conductivity of Tissue Layers.....	13
3. Verification of conformal FDTD scheme implemented in SEMCAD-X.....	16
3.1) Disk Dipole Antenna.....	17
3.2) Spiral Antenna.....	20
4. Parametric Studies- Results and Discussion.....	22
4.1) Methodology.....	22
4.2) Simulation Model Verifications.....	24
4.2.1 Thickness of Muscle Layer.....	25
4.2.2 The Effect of Spatial Resolution on the Skin Layer.....	27
4.3) Dipole Antenna.....	30
4.3.1 The Effect of Insulation Layer around the Dipole Antenna.....	30
4.3.2 The Effect of Fat Layer Thickness.....	33
4.3.3 The Effect of Antenna Embedded in Different Tissue Layers.....	36
4.3.4 Dipole Antenna with Different Length.....	39
4.4) Spiral Antenna.....	41
4.4.1 Effect of Incident Wave Polarization	41
4.5) Impedance Consideration – Dipole and Spiral Antenna.....	43
4.5.1 Cole-Cole to Debye model Conversion for Dispersive Material.....	43
4.5.2 Impedance of Dipole and Spiral Antenna.....	45
5. Conclusions and Directions for Future Work.....	47
References.....	49

Appendix A	Related Publication - Advantage of Modeling Broadband Antennas with “SENCAD X” FDTD Conformal Solver.....	52
Appendix B	Matlab script used to calculate the magnitude of electric field as a function of z (depth into tissue layers).....	59
Appendix C	Matlab script used to convert Cole-Cole model to Debye model for SEMCAD-X by Minimum Square Error curve fitting.....	62

List of Figures

2.1	Sayaka from RF System Lab [11].....	3
2.2	Human head model [12].....	5
2.3	Decomposition of wire antenna with local coordinate rotation [12].....	6
2.4	FDTD Yee's cell [17].....	8
2.5	Excitation signals in SEMCAD-X (a) Broadband simulation excitation signal and (b) Harmonic simulation excitation signal.....	10
2.6	Circumference antenna and its variations [18].....	12
3.1	Illustration of a curved antenna edge modeled using (a) conformal grid and (b) the conventional staircase grid [29].....	16
3.2	Geometry, dimension and orientation of the simulated disk dipole antenna [29].....	17
3.3	Simulated S11 using SEMCAD-X staircase FDTD solver and conformal FDTD solver shown together with the HFSS result as reference.....	17
3.4	SEMCAD-X simulation results with various time step size reduction factors.....	18
3.5	SEMCAD-X simulation results with a coarse grid [29].....	19
3.6	Geometry and dimension of the simulated spiral antenna.....	20
3.7	Simulated S11 (normalized with 188Ω) using SEMCAD-X staircase FDTD solver and conformal FDTD solver shown together with the HFSS result as reference.....	21
4.1	Three-layer tissue model: (a) Top view of the three-layer tissue model (b) side view of the three-layer tissue model (c) 3-D view of the three-layer tissue model	25
4.2	Magnitude of electric field as a function of depth into tissue layer when illuminated by a normal incident plane-wave at (a) 403.5MHz and (b) 6.5GHz with different muscle thickness.....	26
4.3	Calculated electric field magnitude using a two-layer skin model and a single-layer skin model at (a) 403.5MHz and (b) 6.5GHz.....	28

4.4	Simulated induced voltage waveform on a voltage sensor using a two-layer skin model and a single-layer skin model at (a) 403.5MHz and (b) 6.5GHz.....	29
4.5	Geometry and dimension of the modeled wire dipole antenna. Above: wire dipole shown in the <i>x-y</i> plane; Below: wire dipole cross-section view.....	30
4.6	Wire dipole antenna with insulation layer. Above: insulated wire dipole shown in the <i>x-y</i> plane; Below: insulated dipole cross-section view.....	31
4.7	Simulated induced voltage on the dipole antenna with and without insulation layer at (a) 403.5MHz and (b) 6.5GHz.....	32
4.8	Simulated induced voltage on the dipole antenna in muscle layer at 6.5GHz with and without insulation.....	33
4.9	Effect of increasing fat layer thickness at 403.5MHz on (a) induced voltage and (b) electric field magnitude.....	34
4.10	Effect of increasing fat layer thickness at 6.5GHz on (a) induced voltage and (b) electric field magnitude.....	35
4.11	Electric field magnitude distribution at 6.5GHz simulated with SEMCAD-X.....	36
4.12	(a) Calculated electric field magnitude and (b) simulated induced voltage waveforms at various locations at 403.5MHz.....	38
4.13	(a) Calculated electric field magnitude and (b) simulated induced voltage waveforms at various locations at 6.5GHz.....	39
4.14	Simulated induced voltage on the open terminals of the 53mm-long dipole and 5mm-long dipole at (a) 403.5MHz and (b) 6.5GHz.....	40
4.15	Geometry and dimension of the simulated spiral antenna. The antenna is modeled to be 70 μ m thick.....	41
4.16	Simulated induced voltage waveforms with a LHCP plane-wave and a RHCP plane-wave at (a) 403.5MHz and (b) 6.5GHz.....	42
4.17	Relative permittivity and conductivity of fat calculated using Cole-Cole model and Debye model.....	44
4.18	Simulated impedance of (a) wire dipole antenna and (b) spiral antenna at both 403.5MHz and 6.5GHz.....	46

List of Tables

2.1	Summary of some existing bio-telemetry systems[5].....	4
2.2	Parameters of different tissue layers at 403MHz and 6.5GH	15
3.1	Spatial resolution setup for spiral antenna simulation.....	21
4.1	Exposure limits set up by various agencies for general public (non controlled environment).....	22
4.2	Simulation setup variables.....	23
4.3	Simulated induced peak voltage at various embedded at 403.5MHz and 6.5GHz.....	39
4.4	Debye parameters used to model tissue materials.....	44
4.5	Summary of the impedance values for dipole and spiral antenna at both 403.5MHz and 6.5GHz.....	46

Chapter 1

Introduction

Recent research has demonstrated the new areas of antenna applications in biological devices [1], [2]. In these applications, the antenna is usually in close proximity with biological structures. In some cases, the antenna is implanted in the body [3], [4]. In particular, our motivation comes from the emerging technology that aims to use telemetric systems for neurophysiological research.

Currently there are limits to the technologies to stimulate and acquire data remotely from a variety of implanted bio-sensors for a relatively long period of time. Alternate technologies include non-telemetric solutions where external cables are used to supply power to the implanted electrodes and to connect the sensor to the data acquisition system. Existing telemetric solutions are not designed specifically to provide significant bandwidth for multi-channel high-bandwidth data collection and the wireless transmission is usually in the centimetre range. In the proposed future telemetric solution, the antenna has dual functionalities including transmitting bio-signals to the data acquisition system as well as receiving microwave energy to power any implanted subsystems. One of the main technical challenges is the design of a miniaturized high-efficiency broadband rectifier-antenna with relatively long lifespan. This requires careful studies of the antenna behaviour in the complex biological tissue structures.

This thesis presents a study of the antenna behaviour in non-homogeneous lossy media using high-precision electromagnetic simulation software. A brief introduction to the finite-difference time-domain (FDTD) method (numerical foundation of the SEMCAD-X tool) is included in Chapter 2 along with the literature review.

In Chapter 3, we present the SEMCAD-X conformal solver treatment of the curved boundaries by a cross-platform comparison with HFSS (finite-element-based tool).

Chapter 4 summarizes parametric simulation results to study induced open-circuit voltage of a simple dipole antenna as well as a spiral antenna in layered tissue-like media with a plane-wave excitation.

Finally in Chapter 5, we make concluding remarks about the work presented here, and point to possible direction for further investigations.

Chapter 2

Background Review

2.1 RF Bio-Telemetry and Antenna Behaviour

A telemetry system is used to collect data at a place that is remote or inconvenient to access. It often utilizes wireless transmitting channels. A typical telemetry system is composed of a data collection subsystem, a multiplexer, a transmitter/receiver, a de-multiplexer and a data processing unit [6]. Telemetry itself has a long history of development over 200 years [7]. It has been widely accepted in the field of military applications (e.g. missile tests) and industrial applications (e.g. power utility monitoring) [7]. However, it is not until the late 1950s that the biologists and physicians started to realize the potential of telemetry for measuring pH and temperature from internal cavities [9]. A series of lectures and demonstrations were organized world-wide by the scientific and engineering communities from 1960s to 1970s [8], contributing to the overall increase of interest in telemetric system. In the following sections, a very brief review and introduction to RF bio-sensing telemetry is presented followed by a section dedicated to a literature survey of antennas embedded in biological tissues.

2.1.1 RF Bio-Telemetry

Telemetric solution has been used in biological sensing as early as the late 1950s in animal tests. These early bio-sensing telemetric systems used Hartley oscillator as the basic RF building block [8]. It has been shown by Mackay and Jacobson in 1957 that a Hartley oscillator can be configured to work as a pressure sensor as well as a temperature sensor in frequency modulation (FM) [8]. Analog pressure information is modulated onto the carrier signal as a small variation of the resonant frequency, while temperature information is represented by a pulse train at a much lower frequency. It is not until 1970s that measurements from human subjects were shown to be feasible for fetal monitoring in utero, electrocardiogram (ECG) telemetry and gastrointestinal pressures [9]. In these applications, bio-sensing telemetry utilizes RF transmitting channels exclusively as it is vital to leave the

subject in his normal physiological and psychological state with as little interference as possible with his normal pattern of activities.

Due to the low data bandwidth required in the early bio-sensing telemetry system, the transmitting/receiving antenna is usually a fairly simple resonant structure. Often, it is a dipole or a loop antenna. In the early systems, antennas were not specifically designed to work in the biologically embedded environment, but they were rather studied in a simplified dielectric medium. The design work emphasized the position, orientation and physical size of the antenna [8] but largely neglected investigations of its interaction with the living (host) tissue. In the early bio-sensing telemetric systems, batteries were used as the primary power source. This often imposed a trade-off in the design of systems for long-range animal experiments, as the engineering solution frequently represented a compromise between transmitter life, size, weight and transmission range [8].

Although the feasibility of using wireless technology to communicate vital signs was demonstrated more than 30 years ago, the above mentioned limitations in system design have greatly delayed its wide deployment in both research and clinical applications until recent advantages in miniaturized, integrated digital system design. In 2000, Gavriel Iddan *et al* demonstrated a wireless capsule capable of recording 5,000 images over a period of 7-8 hours and transmit the images back to a wearable antenna array [10]. This system had a huge impact on scientists and physicians who were puzzled by the small intestine which was extremely difficult to study using the traditional scope test due to the complicated convolution. In 2005, RF System Lab announced its next generation wireless capsule endoscopy (codename Sayaka) which uses RF inductive power instead of the harmful battery and it is capable to transmit 870,000 images for its 8 hours lifecycle [11]. A sketch of this capsule, demonstrating its dimensions, is shown in Figure 2.1.

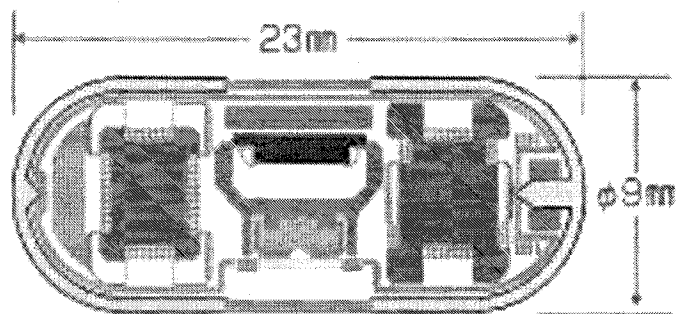


Figure 2.1 Sayaka from RF System Lab [11].

Miniaturized bio-sensing telemetry also finds its use in physiological studies. This has been a particular interest to the National Aeronautics and Space Administration (NASA) where scientists and engineers are trying to develop telemetric-based implantable sensing systems to monitor the physiological parameters of astronauts during space flights [5]. These related researches also utilize inductive power as the energy source for the sensor system. Some examples of resulting bio-sensing telemetric systems are summarized in Table 2.1.

Table 2.1 Summary of some existing bio-telemetric systems.

On-Chip Inductor Dimensions (mm)	Wireless Link Distance (mm)	Reference
2 x 10	30	Von Arx and Najafi [5]
5 x 5	5	Eggers et al. [5]
10.3 diameter	30	Ullerich et al. Mokwa and Schnakenberg [5]
1 x 1	100	Rainee et al. [5]

Notice that the existing systems above only have very short transmission ranges in the order of $1/10^{\text{th}}$ of a meter making them not suitable in some cases where relatively long transmission ranges are required. Due to the relative low operating frequency (VHF band), a square spiral loop is used as the inductor/antenna combination where the ideas of transformer are more relevant than the usual considerations of radiation fields [8].

The proposed new system will operate at a higher frequency to provide wider data bandwidth with an extended transmission range in the order of meter. In 1999, Federal Communications Commission (FCC) and European Telecommunications Standards Institute (ETSI) standardized Medical Implant Communication Service (MICS) band at 402-405MHz. This frequency band is carefully chosen to avoid interference with other RF traffic and to minimize the coupling with living tissues. Implanted antennas have also being designed to operate in the 2.4GHz ISM band. However, due to the high water content in living tissues, the 2.4GHz band has a relatively high conduction loss; therefore it is not a favourable choice for implanted antennas. Last proposed frequency band is at 6.5GHz ISM band [32]. This frequency has the minimum tissue attenuation. In the following section, a

brief literature survey of these biologically-embedded antennas is presented after an introduction to the two common numerical methods used to model these antennas.

2.1.2 Numerical Analysis of Embedded Antenna in Biological Tissue

Antennas used in bio-sensing telemetry function differently from the traditional free-space operation. Their behaviour must be studied in a manner that includes the complex biological environment and its interaction with the near-field antenna radiation. In the literature, biological embedded environment is often modeled as a lossy material with high permittivity. Two numerical methods are commonly used in the analysis. In this section, we present a brief introduction to both of these two methods followed by some published example antenna analysis results.

2.1.2.1 Spherical Dyadic Green's Functions (DGF)

Spherical DGF is often used to model wire antennas in the human head. In this method, the human head is represented by a multi-layer lossy dielectric sphere as shown in Figure 2.2.

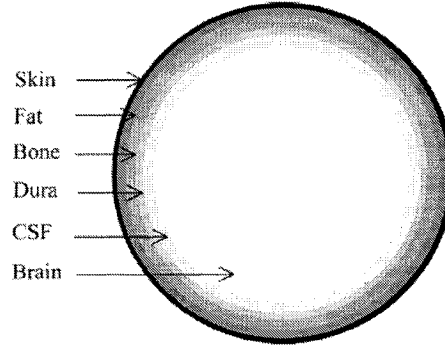


Figure 2.2 Human head model [12].

The total electric field \bar{E} , generated by current density of the implanted source \bar{J}_s , can be calculated by the volume integration over the source in terms of the spherical dyadic Green's Functions

$$\bar{E}_f(\bar{r}) = -j\omega\mu_s \iiint_v [\bar{G}_{e0}(\bar{r}, \bar{r}') \delta_{fs} + \bar{G}_{es}^{(fs)}(\bar{r}, \bar{r}')] \cdot \bar{J}_s(\bar{r}') dV' \quad (2.1)$$

where μ_s is the permeability of the source layer,

$\bar{r}(r, \theta, \varphi)$ is the field location,

$\vec{r}'(r_0, \theta_0, \varphi_0)$ is the source location,

δ_{fs} is the Kronecker delta function,

$\overline{\overline{G_{e0}}}(\vec{r}, \vec{r}')$ is an unbounded spherical DGF in the source region, and

$\overline{\overline{G_{es}^{(fs)}}}(\vec{r}, \vec{r}')$ is a scattering spherical DGF in the field layer from the source.

The detailed derivation of the formulation together with the expressions of $\overline{\overline{G_{e0}}}(\vec{r}, \vec{r}')$ and $\overline{\overline{G_{es}^{(fs)}}}(\vec{r}, \vec{r}')$ can be found in [13], [14], results are also summarized in [12].

To facilitate the numerical implementation of Equation 2.1, the wire antenna is decomposed to represent a superposition of infinitesimal current elements lining up along the antenna. Each infinitesimal current is then decomposed into a rotated local coordinate system as shown in Figure 2.3.

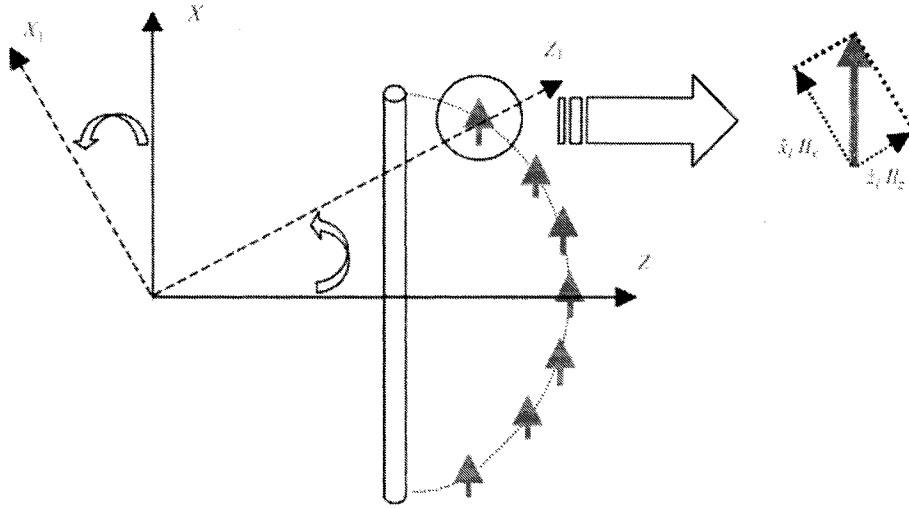


Figure 2.3 Decomposition of wire antenna with local coordinate rotation [12].

Then, the source integration in Equation 2.1 can be approximated by a finite summation of the electric field contributions from all current elements. Each one of the current element contributes to the total electric field by:

$$\begin{aligned} \overline{\overline{E_f}}(\vec{r}) &= -j\omega\mu_f \left[\overline{\overline{G_{e0}}}(\vec{r}, \vec{r}')\delta_{fs} + \overline{\overline{G_{es}^{(fs)}}}(\vec{r}, \vec{r}') \right] \cdot [\hat{x}_1 l_x + \hat{z}_1 l_z] \\ &= \overline{\overline{E_x^i}}(\vec{r}) + \overline{\overline{E_x^s}}(\vec{r}) + \overline{\overline{E_z^i}}(\vec{r}) + \overline{\overline{E_z^s}}(\vec{r}) \end{aligned} \quad (2.2)$$

where $\overline{E}_x^i(\overline{r}_l)$ and $\overline{E}_x^s(\overline{r}_l)$ are the incident and scattering electrical fields from the x -directed infinitesimal current element. $\overline{E}_z^i(\overline{r}_l)$ and $\overline{E}_z^s(\overline{r}_l)$ are the incident and scattering electrical fields from the z -directed infinitesimal current element.

Incident fields $\overline{E}_x^i(\overline{r}_l)$ and $\overline{E}_z^i(\overline{r}_l)$ can be found directly using analytic solution of an infinitesimal electric dipole while scattering electric fields $\overline{E}_x^s(\overline{r}_l)$ and $\overline{E}_z^s(\overline{r}_l)$ can be calculated as following [12]:

$$\overline{E}_x^s(\overline{r}_l) = -j\omega\mu_f l_x \overline{\overline{G}}_{es}^{(fs)}(\overline{r}_l, \overline{r}_l') \cdot \hat{\theta} = -\left(\frac{\omega\mu_f l_x}{4\pi}\right) \frac{1}{r_l'} \sum_{n=1}^{\infty} \frac{(2n+1)}{n(n+1)} \quad (2.3)$$

$$\times \left[\begin{aligned} &(1-\delta_{fN})\overline{M}_{01n}^{(4)}(\beta_f)[A_{n,f}(1-\delta_{SN})\rho_{r_l'} Z_{(n)}^{(4)}(\rho_{r_l}') + B_{n,f}(1-\delta_{S1})\rho_{r_l'} Z_{(n)}^{(1)}(\rho_{r_l}')] \\ &+(1-\delta_{fN})\overline{N}_{e1n}^{(4)}(\beta_f)[C_{n,f}(1-\delta_{SN})\frac{\partial[\rho_{r_l}' Z_{(n)}^{(4)}(\rho_{r_l}')]}{\partial(\rho_{r_l}')} + D_{n,f}(1-\delta_{S1})\frac{\partial[\rho_{r_l}' Z_{(n)}^{(1)}(\rho_{r_l}')]}{\partial(\rho_{r_l}')}] \\ &+(1-\delta_{f1})\overline{M}_{01n}^{(1)}(\beta_f)[E_{n,f}(1-\delta_{1N})\rho_{r_l}' Z_{(n)}^{(4)}(\rho_{r_l}') + F_{n,f}(1-\delta_{S1})\rho_{r_l}' Z_{(n)}^{(1)}(\rho_{r_l}')] \\ &+(1-\delta_{f1})\overline{N}_{e1n}^{(1)}(\beta_f)[G_{n,f}(1-\delta_{SN})\frac{\partial[\rho_{r_l}' Z_{(n)}^{(4)}(\rho_{r_l}')]}{\partial(\rho_{r_l}')} + H_{n,f}(1-\delta_{S1})\frac{\partial[\rho_{r_l}' Z_{(n)}^{(1)}(\rho_{r_l}')]}{\partial(\rho_{r_l}')}] \end{aligned} \right]$$

where $\rho_{r_l}' = \omega\sqrt{\mu_s\epsilon_s(1-\frac{j\sigma_s}{\omega\epsilon_s})}r_l'$ and

$$\overline{E}_z^s(\overline{r}_l) = -j\omega\mu_f l_z \overline{\overline{G}}_{es}^{(fs)}(\overline{r}_l, \overline{r}_l') \cdot \hat{r}_l = -\left(\frac{\omega\mu_f l_z}{4\pi}\right) \frac{1}{r_l'} \sum_{n=1}^{\infty} (2n+1) \quad (2.4)$$

$$\times \left[\begin{aligned} &(1-\delta_{fN})\overline{N}_{e0n}^{(4)}(\beta_f)[C_{n,f}(1-\delta_{SN})Z_{(n)}^{(4)}(\rho_{r_l}') + D_{n,f}(1-\delta_{S1})Z_{(n)}^{(1)}(\rho_{r_l}')] \\ &+(1-\delta_{f1})\overline{N}_{e0n}^{(1)}(\beta_f)[G_{n,p}(1-\delta_{SN})Z_{(n)}^{(4)}(\rho_{r_l}') + H_{n,f}(1-\delta_{S1})Z_{(n)}^{(1)}(\rho_{r_l}')] \end{aligned} \right]$$

where $[A_{n,f}, B_{n,f}, \dots, H_{n,f}]$ are unknown coefficients determined by boundary conditions,

$\overline{M}_{emn}^{(i)}$ and $\overline{N}_{emn}^{(i)}$ are the spherical vector wave functions,
 $Z_{(\beta r)}^{(1)}$ and $Z_{(\beta r)}^{(4)}$ are Bessel and Hankel functions.

Spherical DGF method is only applicable to wire antennas embedded in the simplified head model. This is due to the fact that the formulation of this method utilizes dyadic Green's functions for spherical wave exclusively. In the next section, we will introduce a much more flexible method known as the Finite-Difference Time-Domain (FDTD) method, which can be used to analyze more complicated antenna structure in arbitrary shaped dielectric settings.

2.1.2.2 Finite-Difference Time-Domain (FDTD Method)

The FDTD method is a popular numerical electromagnetic modeling technique. It solves Maxwell's curl equations explicitly by discretizing the problem in both the time domain and the spatial domain. The finite difference technique is applied to update both \bar{E} and \bar{H} field in a leap-frog scheme [15], [16].

Maxwell's curl equations relate the spatial derivative and the time derivative of electric and magnetic fields as follows:

$$\frac{\partial \bar{H}}{\partial t} = -\frac{1}{\mu} \nabla \times \bar{E} - \frac{\rho'}{\mu} \bar{H} \quad (2.5)$$

$$\frac{\partial \bar{E}}{\partial t} = \frac{1}{\varepsilon} \nabla \times \bar{H} - \frac{\sigma}{\varepsilon} \bar{E} \quad (2.6)$$

Where \bar{E} is the electric field intensity in V/m, \bar{H} is the magnetic field intensity in A/m, ε is the electrical permittivity in F/m, μ is the magnetic permeability in H/m, σ is the electrical conductivity in S/m, ρ' is the equivalent magnetic resistivity in Ω /m. Notice that \bar{E} and \bar{H} are vectors of three orthogonal components, therefore each of the above equations can be decomposed into three scalar equations.

\bar{E} and \bar{H} components are positioned along the side of the unit lattice cell as shown in Figure 2.4. In the primary grid, the magnetic field is computed by using the circulating electric fields (implementing thereby directly Ampère's law for that specific grid cell). In the secondary grid, the electric field is computed using the circulating magnetic fields (implementing Faraday's law of induction for that specific grid cell).

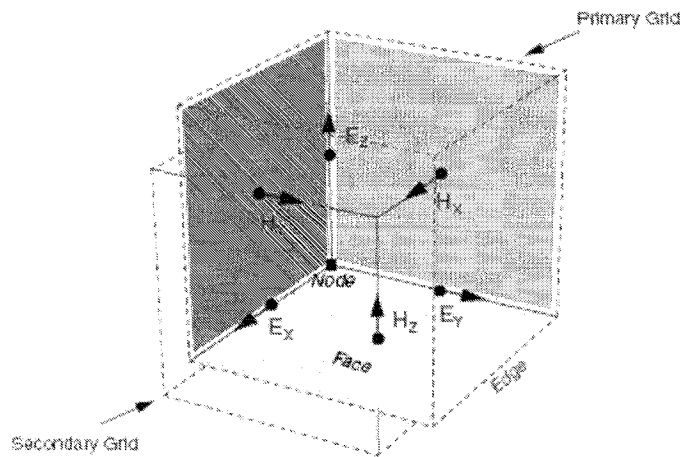


Figure 2.4 FDTD Yee's cell [17].

Using finite difference scheme, the first-order spatial derivate and time derivative reads:

$$\frac{\partial F(i, j, k, n)}{\partial x} = \frac{F|_{i+1/2, j, k}^n - F|_{i-1/2, j, k}^n}{\delta x} + O[\delta x^2] \quad (2.7)$$

$$\frac{\partial F(i, j, k, n)}{\partial t} = \frac{F|_{i, j, k}^{n+1/2} - F|_{i, j, k}^{n-1/2}}{\delta t} + O[\delta t^2] \quad (2.8)$$

With F^n as the electric (\bar{E}) or magnetic (\bar{H}) field at time $n \cdot \delta_t$, where δ_t is the time step. (i, j, k) are the indices of the spatial lattice. $O[(\delta x)^2]$ and $O[(\delta t)^2]$ are high order error terms.

Using Equation 2.7 - 2.8, together with linear approximation: $E_x|_{i, j, k}^{n+1/2} \approx \frac{E_x|_{i, j, k}^{n+1} + E_x|_{i, j, k}^n}{2}$

Equation 2.5 and 2.6 are discretized component-wisely:

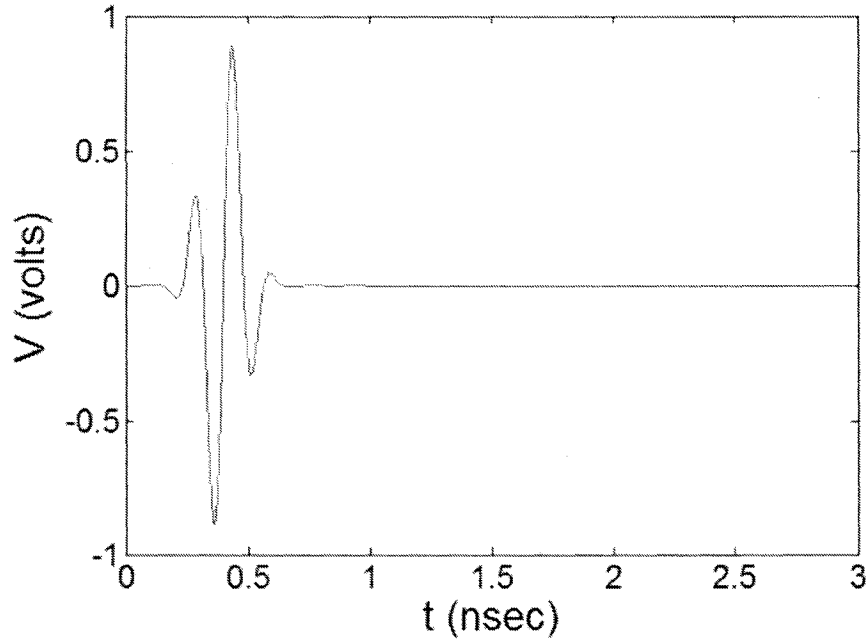
$$H_x|_{i, j, k}^{n+1/2} = \left(\frac{1 - \frac{\Delta t \rho'_{i, j, k}}{2\mu_{i, j, k}}}{1 + \frac{\Delta t \rho'_{i, j, k}}{2\mu_{i, j, k}}} \right) H_x|_{i, j, k}^{n-1/2} + \left(\frac{\Delta t}{1 + \frac{\Delta t \rho'_{i, j, k}}{2\mu_{i, j, k}}} \right) \left[\frac{E_z|_{i, j+1/2, k}^n - E_z|_{i, j-1/2, k}^n}{\Delta y} - \frac{E_y|_{i, j, k+1/2}^n - E_y|_{i, j, k-1/2}^n}{\Delta y} \right] \quad (2.9)$$

and

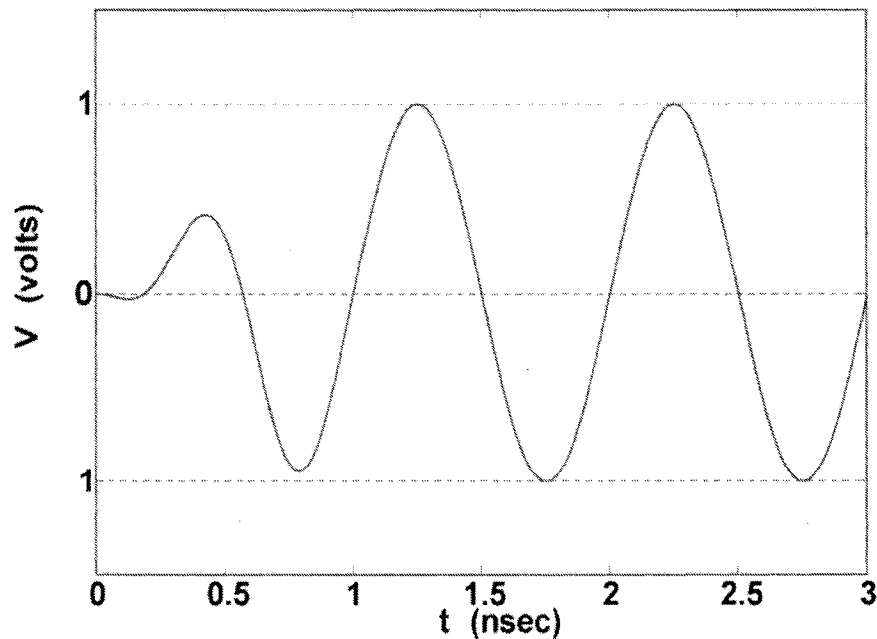
$$E_x|_{i, j, k}^{n+1} = \left(\frac{1 - \frac{\Delta t \sigma_{i, j, k}}{2\varepsilon_{i, j, k}}}{1 + \frac{\Delta t \sigma_{i, j, k}}{2\varepsilon_{i, j, k}}} \right) E_x|_{i, j, k}^n + \left(\frac{\Delta t}{1 + \frac{\Delta t \sigma_{i, j, k}}{2\varepsilon_{i, j, k}}} \right) \left[\frac{H_z|_{i, j+1/2, k}^{n+1/2} - H_z|_{i, j-1/2, k}^{n+1/2}}{\Delta y} - \frac{H_y|_{i, j, k+1/2}^{n+1/2} - H_y|_{i, j, k-1/2}^{n+1/2}}{\Delta y} \right] \quad (2.10)$$

Computational domain in FDTD must be truncated in both the time domain and the spatial domain. In time domain, broadband simulation is terminated when the excitation signal dies out as shown in Figure 2.5(a). This broadband excitation signal is a Gaussian modulated sinusoidal pulse chosen for its flat spectrum content across all frequencies.

Responses at any arbitrary frequencies can be simulated with one simulation run. This is a significant advantage of FDTD over the frequency-domain numerical methods. For harmonic simulations, the excitation signal is a ramped sinusoidal which terminates itself after a user-defined period of simulation time.



(a) Broadband simulation excitation signal



(b) Harmonic simulation excitation signal

Figure 2.5 Excitation signals in SEMCAD-X.

In spatial domain, Absorbing Boundary Conditions (ABC) are necessary to truncate the problem to a finite-size computational domain. In all our simulations, the ABCs are perfectly matched layers (PML).

To guarantee a stable solution in FDTD method, the time evolution step size (δ_t) must be upper bounded by the Courant-Friedrich-Levy (CFL) criterion. For Maxwell's equations, this constraint is:

$$\delta_t \leq \frac{1}{c \sqrt{\frac{1}{\delta x^2} + \frac{1}{\delta y^2} + \frac{1}{\delta z^2}}} \quad (2.11)$$

Where δx , δy and δz are the minimum steps size in x -, y - and z -direction of a Cartesian coordinate system and c is the speed of light in the material of a cell.

2.1.2.3 Sample Studies of Antenna Behaviour in Embedded Environment

Several types of antennas embedded in the human tissue have been studied using FDTD method. In the following section, the antennas are all designed to operate in MICS band at 403.5 MHz. This section presents a brief digest of relevant antennas found in [18].

- *Wire Antenna*

One of the antennas used for implants is an embedded simple wire antenna. The impedance of the antenna is determined by the length of the antenna together with the reflection from the far end [18]. One way to reduce the attenuation introduced is to use insulation around the antenna because the lossy material is then removed from the close proximity region of the strong near-field [18]. To reduce the reflection, an electrical path is established by connecting the far end of the antenna to the living tissue. This structure then becomes the well-known case of travelling wave antenna. The main drawback for this solution is that the characteristics of the antenna vary considerably as the electrical properties of the living tissue varies [18].

- *Circumference Antenna and Variations*

Circumference antenna is popularly used in heart pacemakers because it naturally conforms to the shape of the device. In this case, the circumference antenna is a variation of a

quarter-wavelength monopole antenna where the pacemaker case serves as the ground [18]. Insulator is used to reduce the attenuation as described in the case of wire antennas. The resonant frequency of the antenna is scaled by $1/\sqrt{\epsilon_r}$, where ϵ_r is the dielectric constant of the material hosting the antenna. The antenna length must be scaled by the same factor to result in the specific electrical size. However, the impedance of the antenna will also be scaled down from approximately 40Ω at resonance to about 5Ω [18]. To increase the bandwidth of the antenna and the impedance at resonance, some classical antenna design techniques can be applied. In Figure 2.6, two variations of circumference antenna are shown together with the original model. In (b), the radiator is made thicker to provide a wider bandwidth. The new design has an increased bandwidth of 33% compare to (a) [18]. In (c), the feed structure is modified to bring the impedance at resonance close to 50Ω [18].

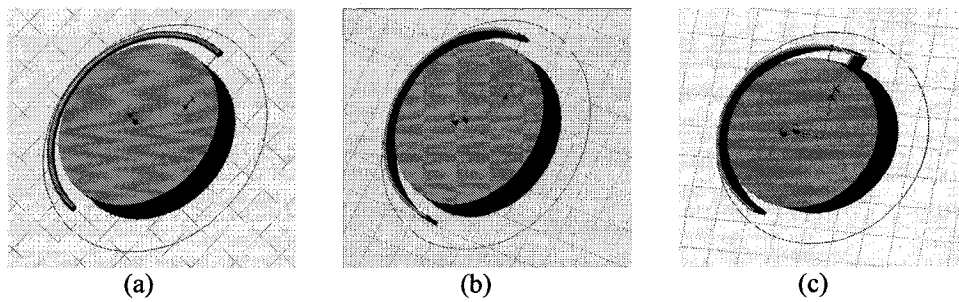


Figure 2.6 Circumference antenna and its variations [18].

- *Patch Antenna*

It has been shown that a patch antenna is not very suitable for implanted devices [18]. The resonance of the structure is compromised by the fact that the antenna is surrounded by conducting tissue materials with high permittivity. To overcome this, a very thick layer of insulation must be used which makes the antenna profile too big to be used in implanted devices.

2.2 Parameters of Tissue Layers

To characterize the behaviour of embedded antenna, several parameters of living tissues must be studied to produce an accurate model. In this section, we present a summary of the

literature survey on related topics. Thickness of different tissue layers can be found in [18], [22] and [23]. Detailed studies of dielectric constants and conductivities of different tissues can be found in [20].

2.2.1 Thickness of Tissue Layers

Depending on the specific applications, antennas are implanted in different organs; therefore they operate in very different environments. One of the most common implanted devices is the pacemaker which is normally implanted directly under patient's skin tissue, typically between the subcutaneous fat tissue and the major pectorals muscle [18]. In the related literatures, these embedded antennas are studied in a three-layer skin-fat-muscle model [21], [22]. The third layer, the muscle tissue, is extending to infinity in the z -direction by using absorbing boundaries.

Notice that each of these three layers has its own complicated structure. For example, the skin tissue is composed of the epidermis, dermis and hypodermis. Each of these sub-layers has slightly different dielectric properties. However, the thickness of each of these sub-layers is much less than a wavelength at either MICS band or ISM band in a dielectric environment with $\epsilon_r = 48$; therefore spatial resolution beyond skin-fat-muscle model is irrelevant. In Chapter 4 of this thesis, we will verify this by comparing the single-layer skin model with a two-layer skin model.

The thickness of different tissue layers varies considerably from individual to individual and from time to time. In literature, skin thickness is normally reported to be in the range from 1mm - 5mm with a typical value close to 3.7mm [2], [12], [18], [22], [23] while the fat layer is usually treated as a parametric variable from 0mm - 15mm [18], [22].

2.2.2 Relative Permittivity and Conductivity of Tissue Layers

Dielectric spectrum of tissues has been well studied and summarized in several publications [20], [24]. In general, *permittivity* ϵ is a complex function of frequency written as:

$$\begin{aligned}\epsilon_c &= \epsilon' - j\epsilon'' && \text{complex permittivity} \\ &= \epsilon_e - j\frac{\sigma_e}{\omega}\end{aligned}\tag{2.12}$$

ϵ_e is the effective permittivity and σ_e is the effective conductivity

Relative permittivity ϵ_{er} is defined as:

$$\epsilon_{er} = \frac{\epsilon_e}{\epsilon_0} \quad (2.13)$$

$$\epsilon_0 = 8.8541878176 \times 10^{12} \text{ F/m}$$

Loss due to finite conductivity is expressed as *loss tangent*

$$\tan \delta = -\frac{\text{Im}[\epsilon_c]}{\text{Re}[\epsilon_c]} = -\frac{\sigma_e}{\omega \epsilon_e} = -\frac{\epsilon''}{\epsilon'} \quad (2.14)$$

Complex permittivity ϵ_c can be approximately expressed as a function of frequency by Debye relaxation expression:

$$\epsilon_c = \epsilon_\infty + j \frac{\epsilon_s - \epsilon_\infty}{1 + j\omega\tau} \quad (2.15)$$

where

ϵ_∞ is the permittivity at the high frequency limit,

ϵ_s is the low frequency (static) permittivity,

τ is the characteristic relaxation time of the medium.

Hurt modeled the dielectric spectrum of the muscle using a summation of five Debye dispersions in addition to a conductivity term as followed [25]:

$$\epsilon_c = \epsilon_\infty + \sum_{n=1}^5 \frac{\Delta\epsilon_n}{1 + j\omega\tau_n} + \frac{\sigma_i}{j\omega\epsilon_0} \quad (2.16)$$

where

τ_n is the n^{th} characteristic relaxation time of the medium

$\Delta\epsilon_n$ is the change in the relative permittivity ($\epsilon_s - \epsilon_\infty$) associated with τ_n

σ_i is the static ionic conductivity

$\Delta\epsilon_1, \Delta\epsilon_2 \dots$ can be normalized respect to one constant $\Delta\epsilon$ and Equation 2.16 becomes

$$\epsilon_c = \epsilon_\infty + (\epsilon_s - \epsilon_\infty) \sum_{n=1}^5 \frac{A_n}{1 + j\omega\tau_n} + \frac{\sigma_i}{j\omega\epsilon_0} \quad (2.17)$$

Due to the complex nature of biological tissues, each of the Debye terms is broadened by introducing an empirical distribution parameter α_n , the result is known as the multi-term Cole-Cole expression:

$$\epsilon_c = \epsilon_\infty + \sum_{n=1}^5 \frac{\Delta\epsilon_n}{(1 + j\omega\tau_n)^{(1-\alpha_n)}} + \frac{\sigma_i}{j\omega\epsilon_0} \quad (2.18)$$

where

α_n is the measure of broadening of the dispersion

All the constants for the Cole-Cole model can be found in [20]; therefore using Equation 2.18, complex permittivity can be calculated at any given frequency. The following values are taken from [26] calculated using Equation 2.18 at 403MHz and 6.5GHz with the exception of the unified skin tissue where the relative permittivity and conductivity are calculated using the weighted average of the dry skin and wet skin over their thickness.

Table 2.2 Parameters of different tissue layers at 403MHz and 6.5GH.

Tissue	403MHz		6.5GHz	
	ϵ_{er}	σ (S/m)	ϵ_{er}	σ (S/m)
Muscle	57.104	0.79708	47.544	5.8201
Fat	5.5785	0.041167	4.8917	0.33955
Skin (dry)	46.718	0.68934	34.519	4.3433
Skin (wet)	49.85	0.67004	37.761	5.0544
Skin (averaged)	48.0603	0.6811	35.91	4.6481

Chapter 3

Verification of Conformal FDTD Scheme Implemented in SEMCAD-X

SEMCAD-X (Schmid and Partner Engineering Company [17]) is a 3-D full-wave simulator based on the Finite-Difference Time-Domain (FDTD) algorithm. In SEMCAD-X, several variations of standard FDTD method are implemented. One of these variations is the conformal FDTD solver. Unlike the standard staircase formulation used to treat the curved boundaries, the conformal FDTD solver treats the media on the two sides of the boundary in a manner that results in a smaller approximation error. In the staircase FDTD algorithm, one cell can only represent one single type of material in contrast to the conformal FDTD, where weighted averages of electrical constants are used for the boundary cells. This allows the discretized boundaries to “follow” the geometric boundaries of the structure more closely as illustrated in Figure 3.1 below.

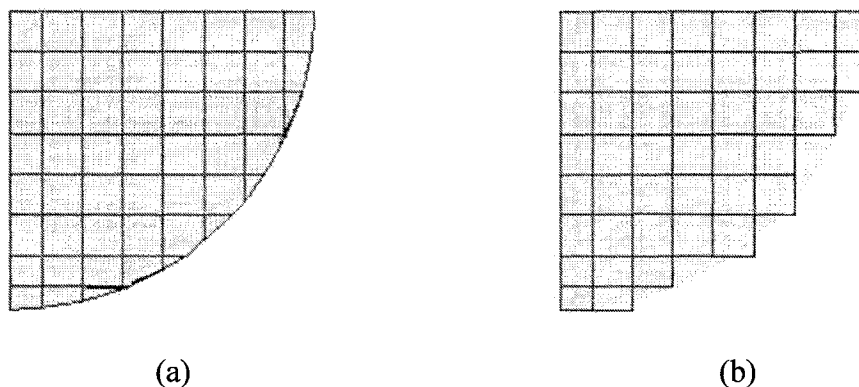


Figure 3.1 Illustration of a curved antenna edge modeled using (a) the conformal grid and (b) the conventional staircase grid [29].

Using the conformal scheme with a coarser spatial resolution produces the same accuracy as a much finer staircase mesh, but with significant savings in memory requirements and simulation time [17]. Two case studies are presented in this section to help understand the characteristics of conformal FDTD solver implemented in SEMCAD-X. The reflection coefficient (S_{11}) was simulated for a disk dipole antenna first and then a spiral antenna.

These two antennas were chosen for their curved boundaries which best differentiate the conformal and the conventional staircase FDTD solvers.

3.1 Disk Dipole Antenna

The geometry of disk dipole antenna is shown in Figure 3.2 together with its dimension and its orientation relative to the coordinate system. The antenna is 70 μm in thickness with 1mm spacing between disks to accommodate the feed structure. The reflection coefficient (S11) was first simulated in HFSS as the reference and then in SEMCAD-X using both conventional staircase FDTD solver and conformal FDTD solver. The simulated S11 in this section is normalized with respect to 50 Ω . The results are shown in Figure 3.3.

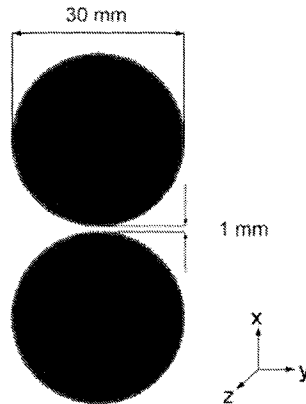


Figure 3.2 Geometry, dimension and orientation of the simulated disk dipole antenna [29].

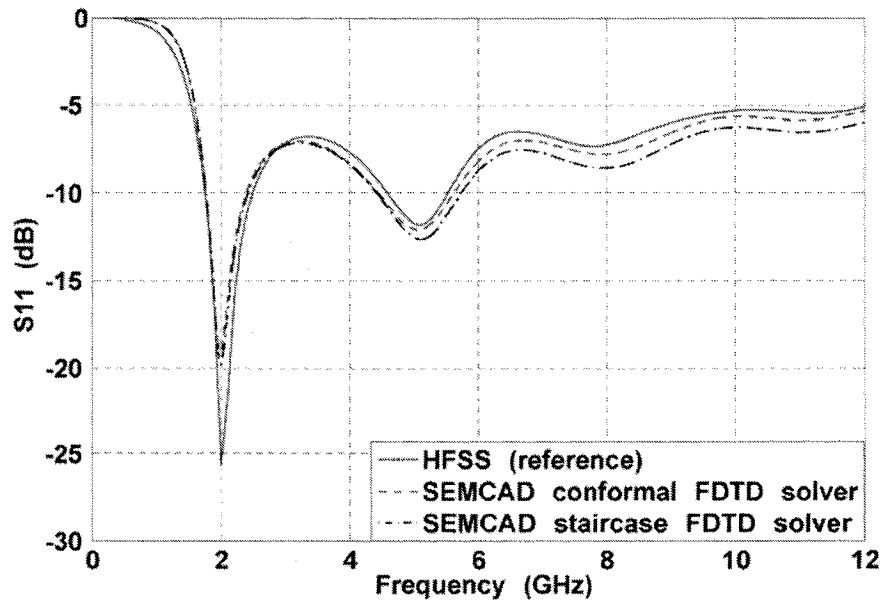


Figure 3.3 Simulated S11 using SEMCAD-X staircase FDTD solver and conformal FDTD solver shown together with the HFSS result as reference.

The same very dense mesh was used for both the staircase FDTD and conformal FDTD. The free-space region was discretized with maximum step 2mm while the minimum step was 0.2mm in x - and y -direction. The step size in the antenna region was uniformly set to 0.2mm in x - and y -direction. In z -direction, the minimum step was uniformly set to 0.035mm and the maximum to 2mm. This grid generated a spatial computational domain of 5 million cells. The simulations were carried out on a Dell Precision 670 computer (Dual-Core 2.80 GHz Intel Xeon, 4 GB DDR2 SDRAM) with an aXware accelerator card [17]. Simulation time was 1:27:34 for the conformal solver and 0:40:22 for the conventional staircase FDTD solver. The longer simulation time for the conformal solver was due to the fact that the time evolution step size was only 50% of the maximum allowed time step size determined by CFL in Equation 2.11. The relatively long simulation time for conformal solver can be significantly improved by using a smaller reduction factor. The simulated S11 results are shown in Figure 3.4 using 50% CFL ($0.5\delta_t$), 70% CFL ($0.7\delta_t$) and 100% CFL (δ_t) with HFSS result as the reference. As shown in Figure 3.4, the simulation maintains accurate even when no time step reduction is used (i.e. 100% CFL).

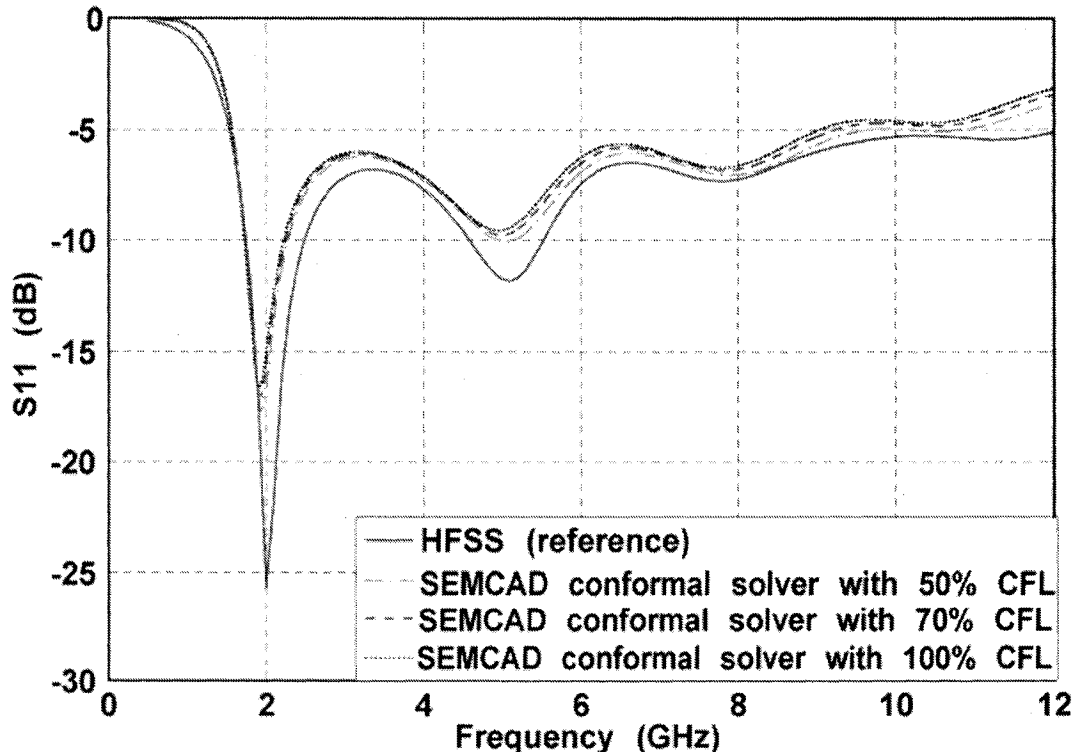


Figure 3.4 SEMCAD-X simulation results with various time step size reduction factors.

A further investigation showed that with conformal solver, a coarse grid can be used instead of the very dense one with acceptably accurate results. The coarse grid was setup to discretize free-space region with maximum step size 2mm while the minimum step size 1mm for both x - and y -direction. The maximum step size in the antenna region was 2mm in x - and y -direction while the minimum step size was 1.5mm in x -direction and 1mm in y -direction. In z -direction, the setup was the same as in previously described study. This grid generated a much smaller spatial computational domain of 0.3 million cells. The simulation result is shown in Figure 3.5 together with the HFSS reference. As a comparison, the conventional FDTD solver is also engaged here with the same coarse grid. The conformal FDTD recovers the solution very well while the conventional FDTD has a progressively increasing error of more than 5dB. The computation time has also dramatically reduced to 0:11:14 with a 50% CFL ($0.5\delta t$) time step reduction. In conclusion, the conformal FDTD solver implemented in SEMCAD-X for treatment of curved boundaries enables remarkable savings in memory requirements and simulation time without compromising any simulation accuracy. In the next section, we will apply this rule to simulate a spiral antenna.

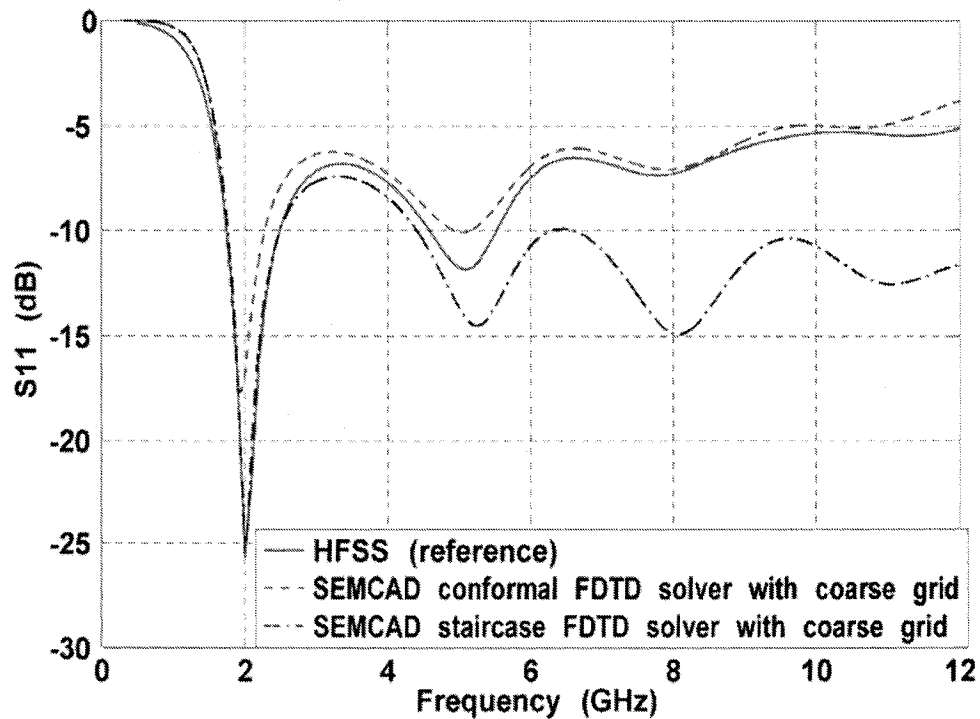


Figure 3.5 SEMCAD-X simulation results with a coarse grid [29].

3.2 Spiral Antenna

Spiral antenna is a self-complementary radiating structure. In theory, the behaviour of a spiral antenna should be independent of frequency. The theoretical impedance of a self-complementary antenna in free-space is:

$$Z_{spiral} = \frac{1}{2} Z_{free_space} = \frac{1}{2} \sqrt{\frac{\mu_0}{\epsilon_0}} = 60\pi \approx 188\Omega \quad (3.1)$$

Due to its complicated curved boundaries, simulation of the spiral antenna is commonly a challenge. In practice, spiral antennas have been suggested for use in the RF energy recycling applications [27]. This recycling RF energy concept may be effectively extended to the embedded bio-telemetric system discussed in Chapter 2 as the main or backup power source. In this section, we simulate spiral antenna in free-space.

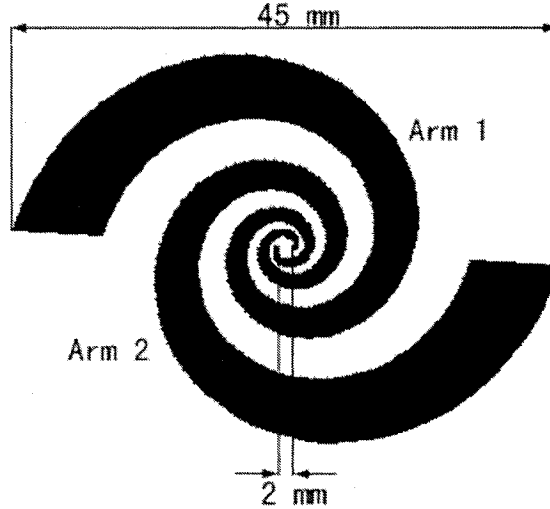


Figure 3.6 Geometry and dimension of the simulated spiral antenna.

The above spiral antenna can be mathematically described as:

$$\text{Arm 1} \begin{cases} r_1 = e^{0.25\varphi} \\ r_2 = e^{0.25(\varphi - \frac{\pi}{2})} \end{cases} \quad \forall 0 \leq \varphi \leq 4\pi$$

$$\text{Arm 2} \begin{cases} r_1 = (r_1, \varphi - \frac{\pi}{2}) \\ r_2 = (r_2, \varphi - \frac{\pi}{2}) \end{cases} \quad \forall 0 \leq \varphi \leq 4\pi$$

The antenna is 35 μ m thick with a 0.508mm thick Rogers Duroid substrate ($\epsilon_r = 2.2$, $\mu_r = 1$).

The reflection coefficient S11 was first simulated in HFSS as the reference and then in

SEMCAD-X using both the staircase FDTD solver with a dense grid and the conformal FDTD solver with a coarser grid. The spatial discretization parameters are summarized in Table 3.1 and the results are graphed in Figure 3.7. The simulation time for the staircase FDTD solver with the dense grid (9.19 million cells) was 8:24:23; while the conformal FDTD solver with the coarse grid (5.35 million cells) and 50% CFL (high accuracy setting) required 4:32:38. The case of the spiral antenna confirmed that the conformal FDTD introduces significant computational time and memory savings with respect to the staircase FDTD scheme.

Table 3.1 Spatial resolution setup for spiral antenna simulation.

	Antenna Region		Free-space Region		Grid size
	Maximum step size (mm)	Minimum step size (mm)	Maximum step size (mm)	Minimum step size (mm)	
Dense	x-dir: 0.1 y-dir: 0.1 z-dir:0.035	x-dir:0.001 y-dir:0.001 z-dir:0.035	x-dir: 0.1 y-dir: 0.1 z-dir:0.01	x-dir:10 y-dir:10 z-dir:10	537x402x80 = 9.19 Mcells
Coarse	x-dir: 0.1 y-dir: 0.1 z-dir:0.035	x-dir:0.3 y-dir:0.3 z-dir:0.035	x-dir:0.1 y-dir:0.1 z-dir:0.01	x-dir:10 y-dir:10 z-dir:10	521x387x64 = 5.35 MCells

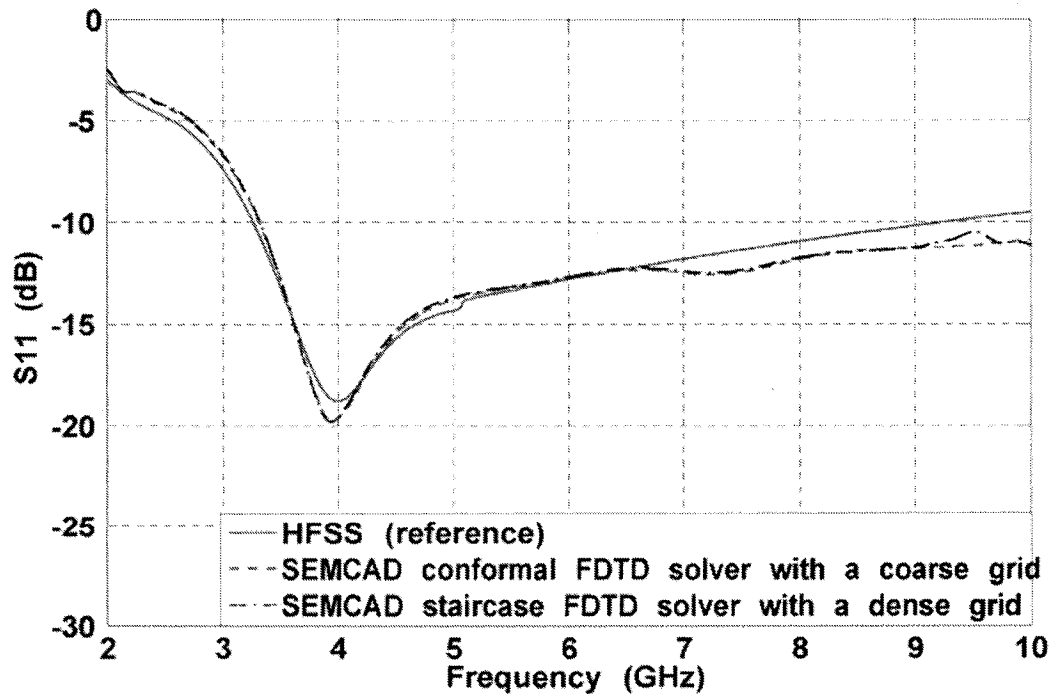


Figure 3.7 Simulated S11 (normalized to 188Ω) using SEMCAD-X staircase FDTD solver and conformal FDTD solver shown together with the HFSS result as reference.

Chapter 4

Parametric Studies- Results and Discussion

Instead of focusing on the radiating characteristics of an antenna, in this section, we focus on its receiving properties. In particular, this antenna will be used as part of the rectifier-antenna (i.e. rectenna). As the name suggests, this structure rectifies the received RF signal to provide its DC component. Therefore, utilizing a rectenna can effectively eliminate external cables or batteries for the embedded bio-telemetric devices and provide internal power source. Preliminary studies of miniaturized rectenna in free-space have been published [27], [30] and [31]. In this thesis, we demonstrate a study of the receiving characteristics of the rectenna in the context of its proximity to the biological tissues. Our test cases are the wire dipole antenna chosen for its structural simplicity and robustness, and the spiral antenna chosen for its wide bandwidth. The incident wave is a plane-wave with specified frequency and magnitude. The excitation frequencies of interest are 403.5MHz and 6.5GHz. The magnitude of electric field is set to 1V/m for all cases. This value is well below electromagnetic field exposure limits set by IEEE, FCC and International Commission on Non-Ionizing Radiation Protection (ICNIRP) outlined in Table 3.1 at both frequencies.

Table 4.1 Exposure limits set up by various agencies for general public (non controlled environment).

	Power density (mW/cm ²)		Equivalent plane wave \bar{E} field amplitude (V/m)	
	403.5MHz	6.5GHz	403.5MHz	6.5GHz
IEEE Std C95.1 [33]	0.269	4.33	31.8	127.8
FCC OET Bulletin 65 [34]	0.269	1.0	31.8	61.4
ICNIRP Std, [35]	0.202	1.0	27.6	61.4

4.1 Methodology

There are several variables of particular interest in terms of their effects on the induced voltage on the receiving antenna terminals. These variables are summarized in Table 4.2. One of the most important parameters is the location where the antenna is embedded. The

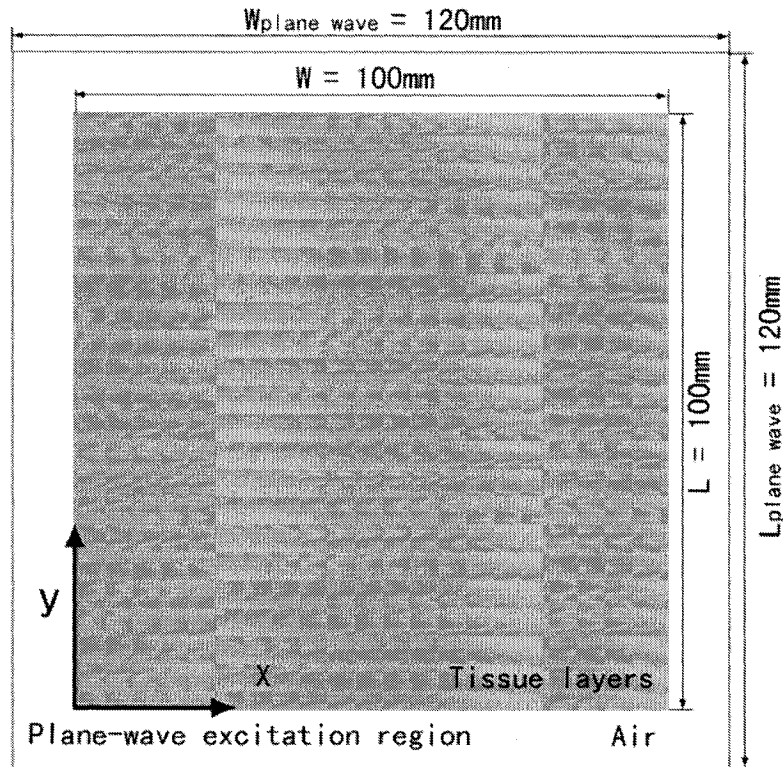
antennas are simulated when placed in different tissue layers: skin, fat and muscle. Within the relatively thick fat layer, we examine the antenna at four different locations relative to its position to the skin/fat interface. For an additional parametric study, we fix the antenna in the skin layer and vary the thickness of the underneath fat layer from 5mm to 20mm to investigate the change of the dielectric distribution in the near-field of the antenna on its properties. Similar procedure has been reported in [18] and [19]. Both the wire dipole and the spiral antenna are simulated for the settings noted above. Our further investigations consider miniaturized dipole and spiral antenna, more appropriate for implant applications. The dipole antenna is scaled down by $1/10^{\text{th}}$ and the spiral antenna by $1/2$ of their initially studied size. In practice, metals are not directly implanted in tissues and thus the study of the insulation layer around the antenna is of particular importance. Literature indicates that the insulation layer can help improve the radiation efficiency when the antenna is embedded in a lossy material [18]. Hence, part of our study focuses on detecting any possible effect of the insulation layer on the induced voltage of the embedded antennas via simulations. Finally, all the simulations are performed at both 403.5MHz and 6.5GHz. We selectively present the representing results from our simulations in section 4.3 and 4.4.

Table 4.2 Simulation setup variables.

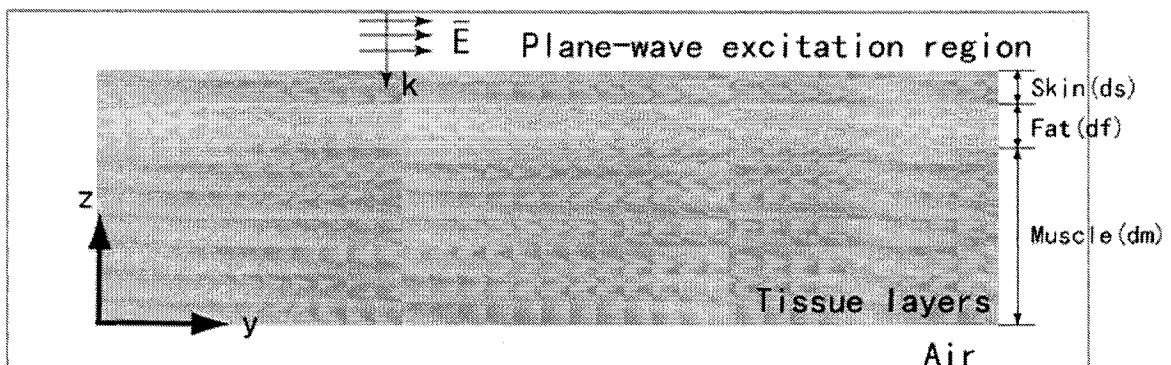
Variable	Value	
Type of antenna	dipole	spiral
Locations of the antenna	one location in skin layer ($z = -1.7\text{mm}$) four locations in fat layer ($z = -5.7, -7.7, -11.7, -19.7\text{mm}$) one location in muscle layer ($z = -25.7\text{mm}$)	
Thickness of fat layer	5mm, 10mm, 20mm	
Insulation layer	with insulation layer	without insulation layer
Size of the antenna	Original: 53mm (length)	Original: 45mm (diameter)
	Scaled: 5.3mm (length)	Scaled: 22.7mm (diameter)
Excitation frequency	403.5MHz	6.5GHz

4.2 Simulation Model Verifications

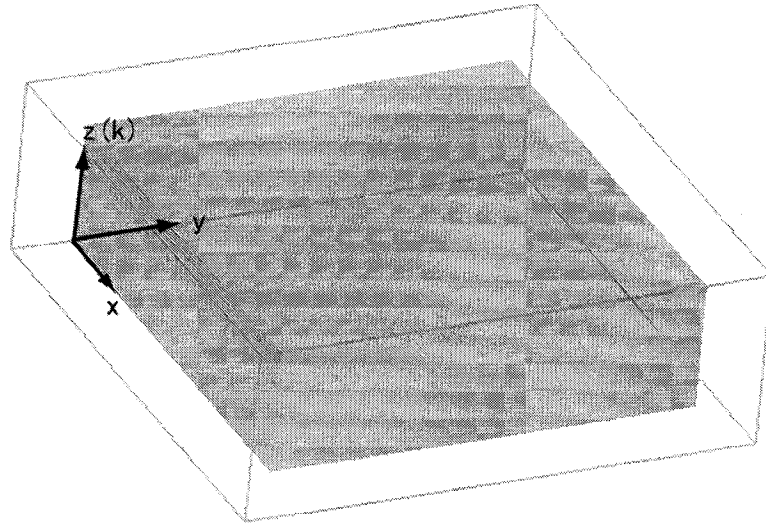
Three-layer tissue model is shown in Figure 4.1. The exciting plane-wave signal is propagating in $-z$ direction (i.e. perpendicular into the plane of the page) within the plane-wave excitation region.



(a) Top view of the three-layer tissue model



(b) Side view of the three-layer tissue model

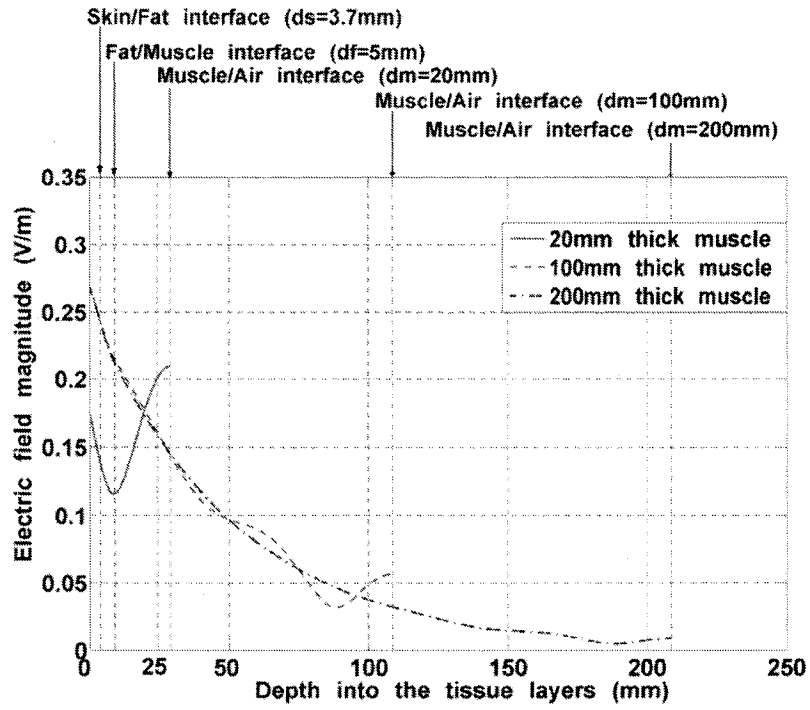


(c) 3-D view of the three-layer tissue model

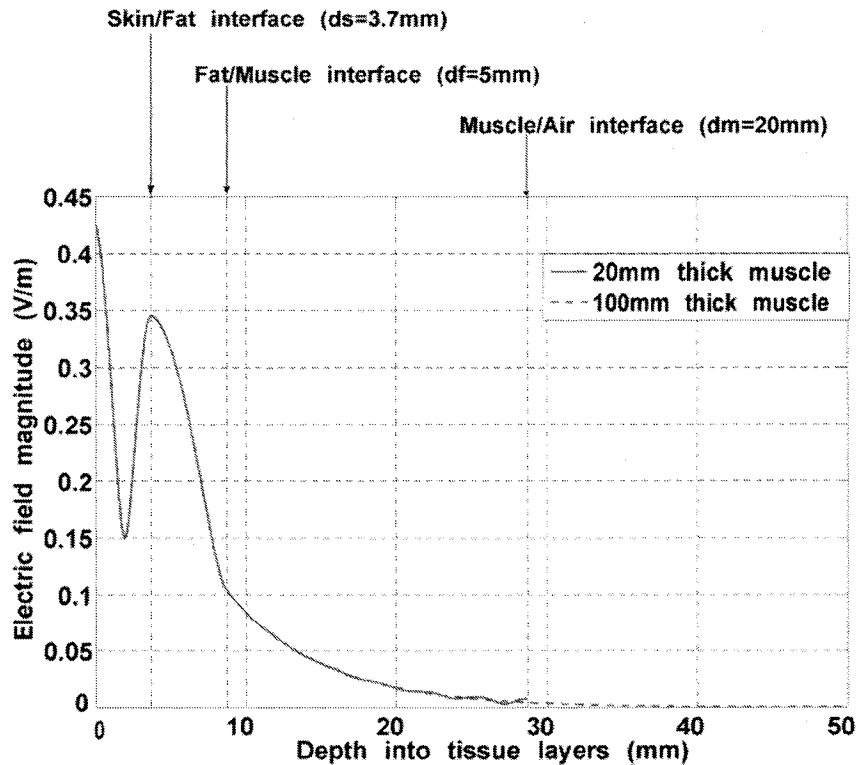
Figure 4.1 Three-layer tissue model.

4.2.1 Thickness of Muscle Layer

Ideally, Absorbing Boundary Conditions (ABCs) should be applied on the four side-walls as well as the bottom face of the model to eliminate reflecting waves. However, due to the limitation of the aXware accelerator card on the computers available, this model cannot be implemented when plane-wave excitation is used. For the side-walls, as the incident wave is propagating in the $-z$ direction, we assume that the reflection from these faces is small enough to be safely neglected as they are mainly reflection of scattering field caused by the embedded antenna structure. To eliminate the reflection from the bottom muscle/air interface, we use a muscle layer with extended thickness such that the conduction loss introduced by the finite conductivity of the muscle consumes most of the wave energy, reducing the reflected wave to a negligible level. To validate the thickness of muscle layer required to safely ignore the reflection from the bottom, a Matlab script is written to calculate the 1-D electric field magnitude as a function of z (depth into the tissues) (see Appendix B). The program utilizes the continuity of tangential electric field and magnetic field on dielectric boundaries to form a set of linear equations. Solving these equations gives the magnitudes of the electric field at these boundaries. The complete solution can then be interpolated according to the theoretical formula. The magnitude of electric field across tissue layers are shown in Figure 4.2.



(a)



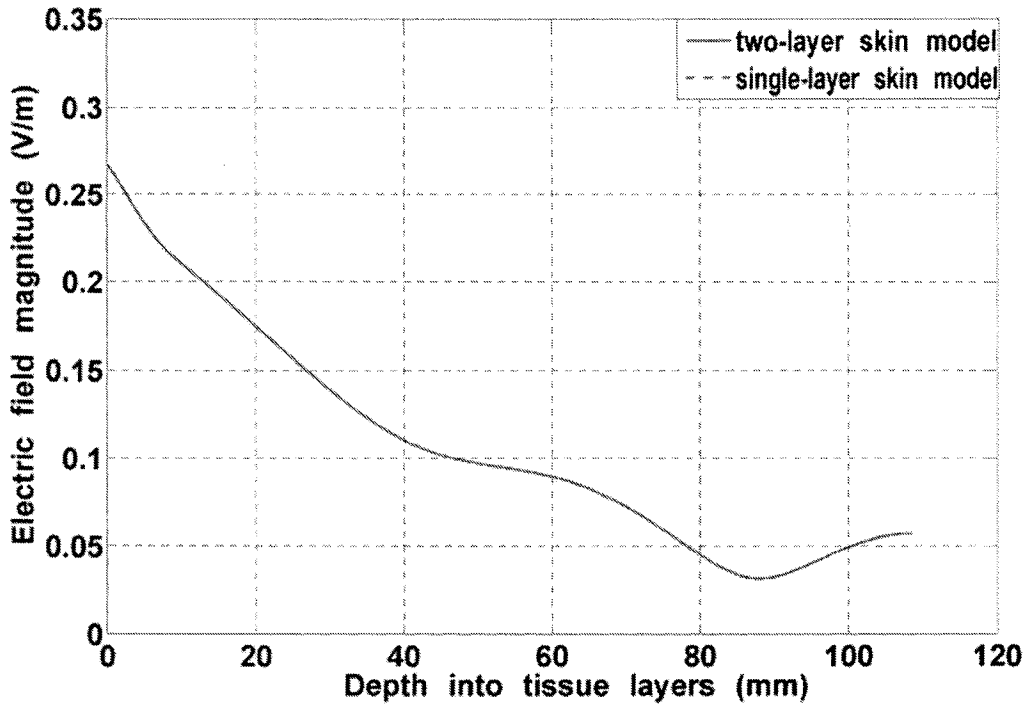
(b)

Figure 4.2 Electric field magnitudes as a function of depth into tissue layer when illuminated by a normal incident plane-wave at (a) 403.5MHz and (b) 6.5GHz with different muscle thickness.

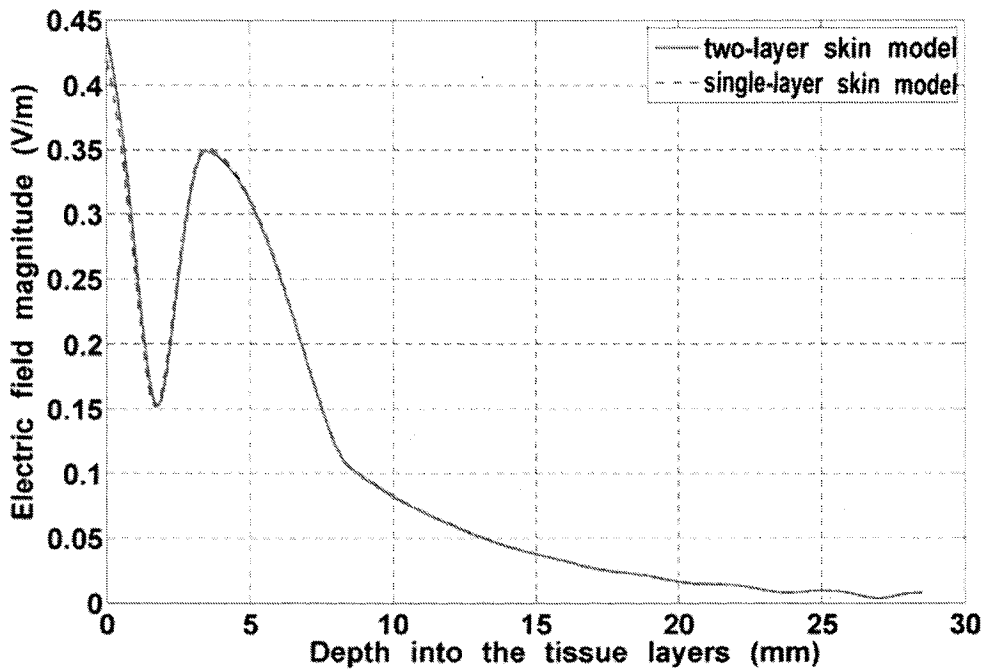
As shown in Figure 4.2(a), at 403.5MHz the magnitude of electric field changes significantly when the thickness of muscle layer varies from 20mm to 100mm. However, the magnitude of electric field does not change very much when the thickness of the muscle layer grows from 100mm to 200mm. This statement is especially true when the magnitude of electric field is measured at depth into the tissues smaller than 25mm. From these results we infer that a 100mm thick muscle layer ($d_m = 100\text{mm}$) is sufficient to eliminate unwanted reflections from the muscle/air interface through the loss mechanism at 403.5MHz. At 6.5GHz, we expect that, due to higher conductivity loss (Table 2.2), a thinner muscle layer should provide sufficient attenuation to safely ignore the reflection from the bottom muscle/air interface. This is clearly confirmed by the overlap of relevant results graphed in Figure 4.2(b). As a conclusion for 6.5GHz, a 20mm thick muscle layer ($d_m = 20\text{mm}$) is sufficient to reduce the reflection from the bottom muscle/air interface to a negligible level and thus emulate the absorbing boundary conditions.

4.2.2 The Effect of Spatial Resolution on the Skin Layer

The skin layer shown in Figure 4.1(b) can be further decomposed into wet skin and dry skin. They have slightly different relative permittivities as shown in Table 2.2. The thickness of wet skin is around 1.5mm and that of the dry skin is approximately 2mm [36]. However, we expect that this marginal increment of spatial resolution on the skin layer should not have a significant effect on our simulations. This statement holds true at both 403.5MHz and 6.5GHz, as the wavelengths corresponding to both frequencies in the dielectric environment are much larger than the thickness of the skin layer. Therefore, the wave can hardly distinguish between wet skin and dry skin. To validate the single-layer skin model, a two-layer skin model is tested for a comparison. The thickness of single-layer skin is 3.7mm ($d_s = 3.7\text{mm}$) with underneath fat layer of 20mm ($d_f = 20\text{mm}$), and the muscle layer has the thickness described in previous section. The magnitude of electric field is again calculated using the Matlab script described in previous section. Results are shown in Figure 4.3. Field calculations confirm that the single-layer skin model with averaged (ϵ_{er}, σ) is accurate enough to model the field distributions at 403.5MHz and 6.5GHz.



(a)

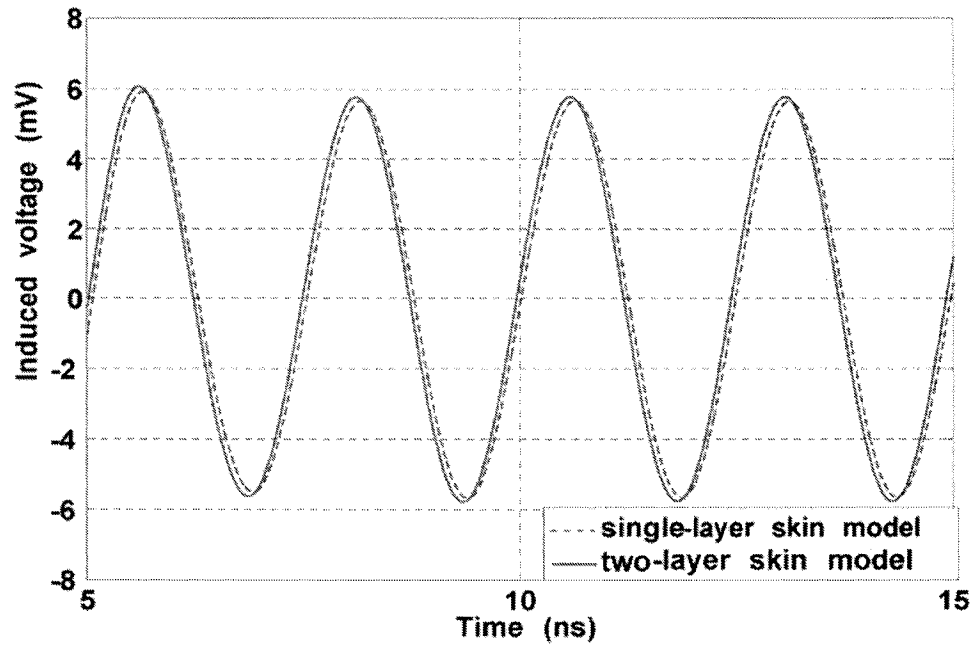


(b)

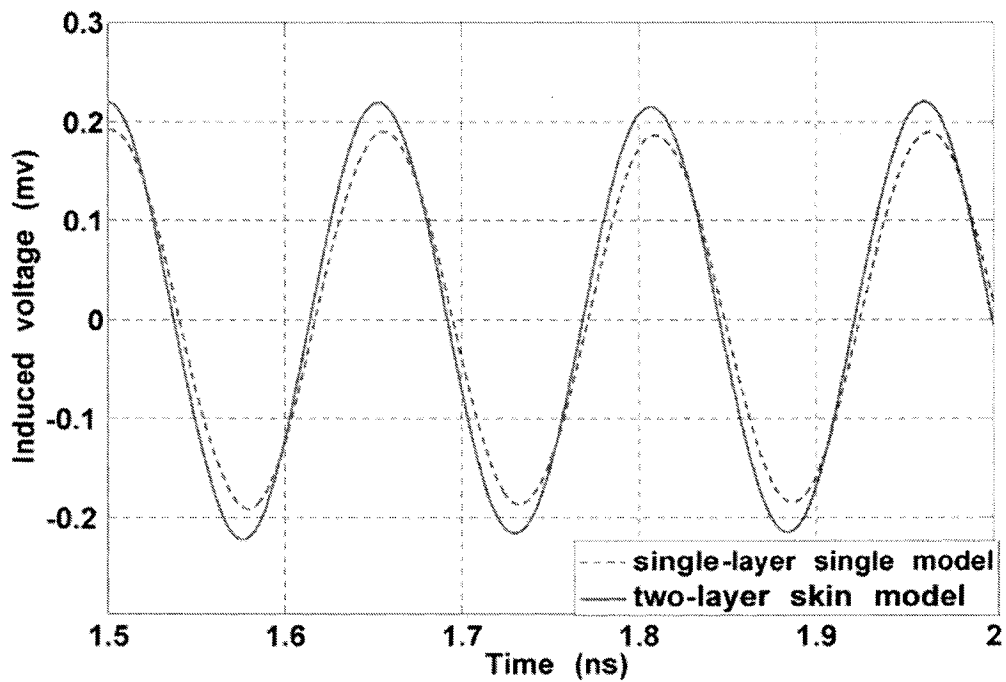
Figure 4.3 Calculated electric field magnitude using a two-layer skin model and a single-layer skin model at (a) 403.5MHz and (b)6.5GHz.

Further simulations in SEMCAD-X confirm that an *ideal voltage sensor* embedded in the single-layer skin model and the two-layer skin model yields practically identical

induced voltage level as shown in Figure 4.4. The voltage sensor is embedded 1.7mm into the skin layer ($z = -1.7\text{mm}$). This again confirms that the detailed, two-layer skin model may not be necessary to use for accurate results.



(a)



(b)

Figure 4.4 Simulated induced voltage waveform on a voltage sensor using a two-layer skin model and a single-layer skin model at (a) 403.5MHz and (b) 6.5GHz.

4.3 Dipole Antenna

In this section, we simulate the induced open-circuit voltage of a small dipole antenna when illuminated by the plane-wave described previously. The dipole antenna is placed in different positions in the layered tissue model as shown in Figure 4.1. The orientation of the dipole is chosen to match the polarization of the incoming plane-wave (i.e. y -oriented). The geometry and dimension of the dipole antenna is shown in the Figure 4.5.

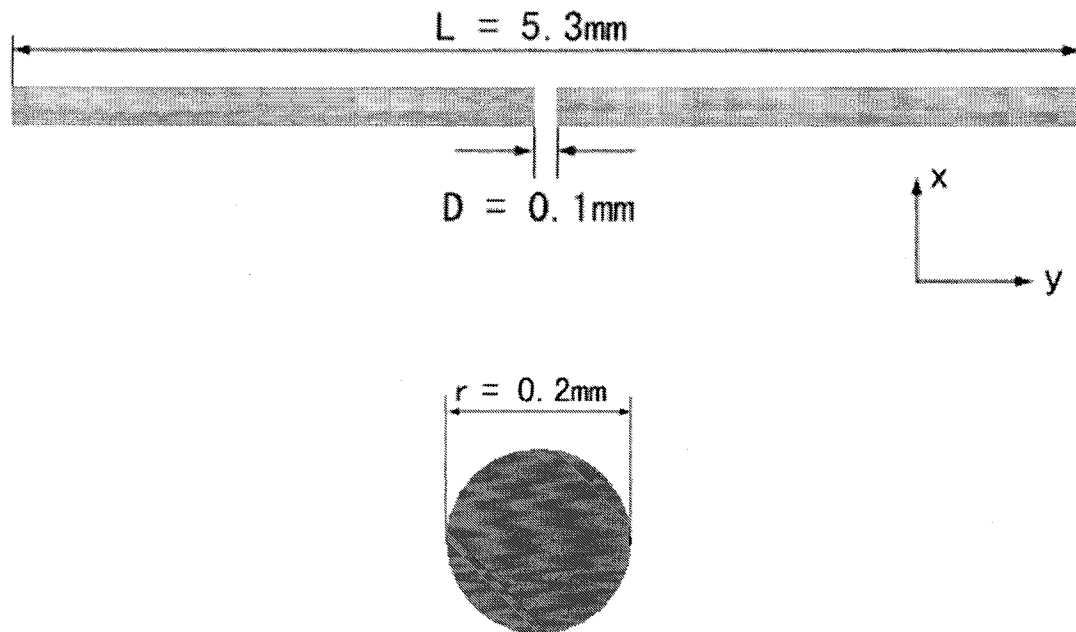


Figure 4.5 Geometry and dimension of the modeled wire dipole antenna. Above: wire dipole shown in the x - y plane; Below: wire dipole cross-section view.

4.3.1 The Effect of Insulation Layer around the Dipole Antenna

Dielectric coating is commonly used to isolate the implanted antenna from the surrounding tissues. Radiation efficiency of the antenna can be improved as the lossy tissue media is removed from the close proximity of the near field region of the radiating antenna. This design principle is applied widely to embedded radiating antennas [18]. In this section, we examine the effect of a such insulation layer, however, we are not concerned about the radiating efficiency improvement, but rather the effect of this insulation layer on the induced open-circuit voltage at the antenna terminals. The dipole antenna with the

insulation layer is shown in Figure 4.6. The inner, metallic section of the antenna has the same dimensions as the one shown in Figure 4.5.

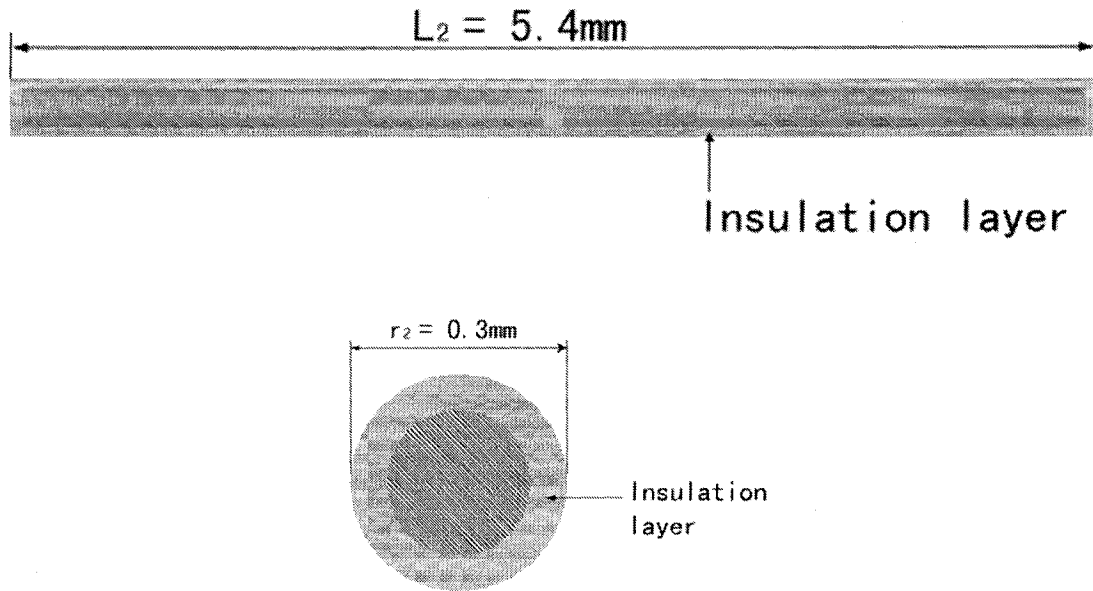
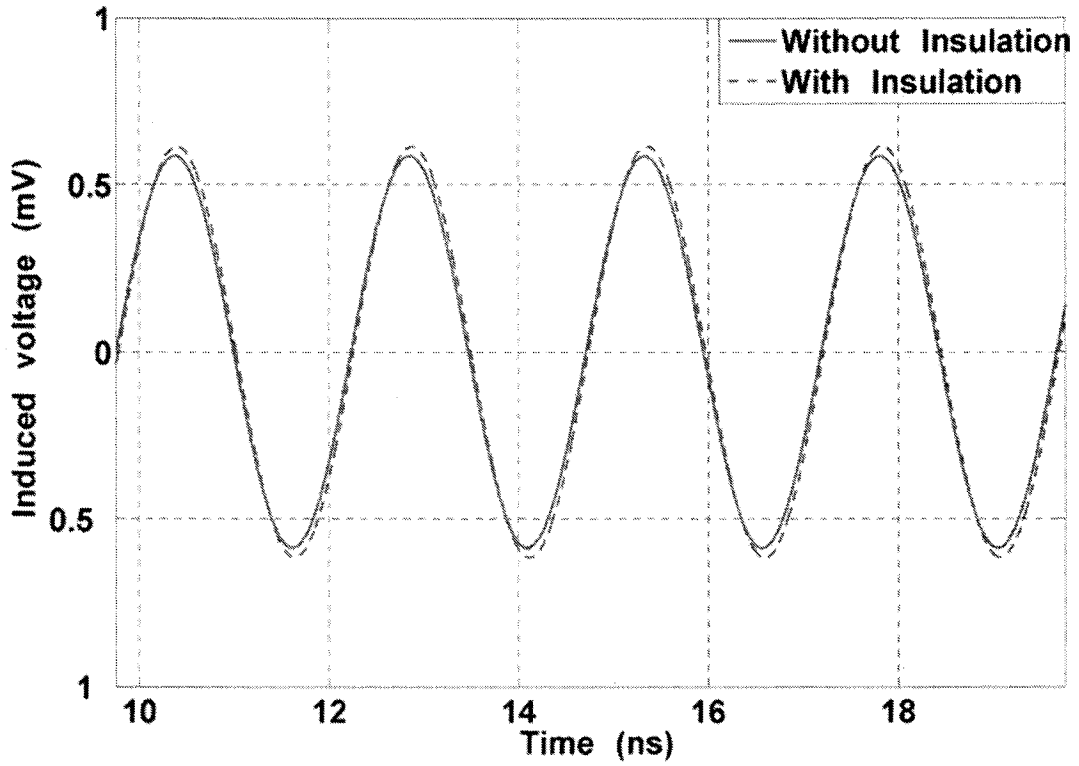
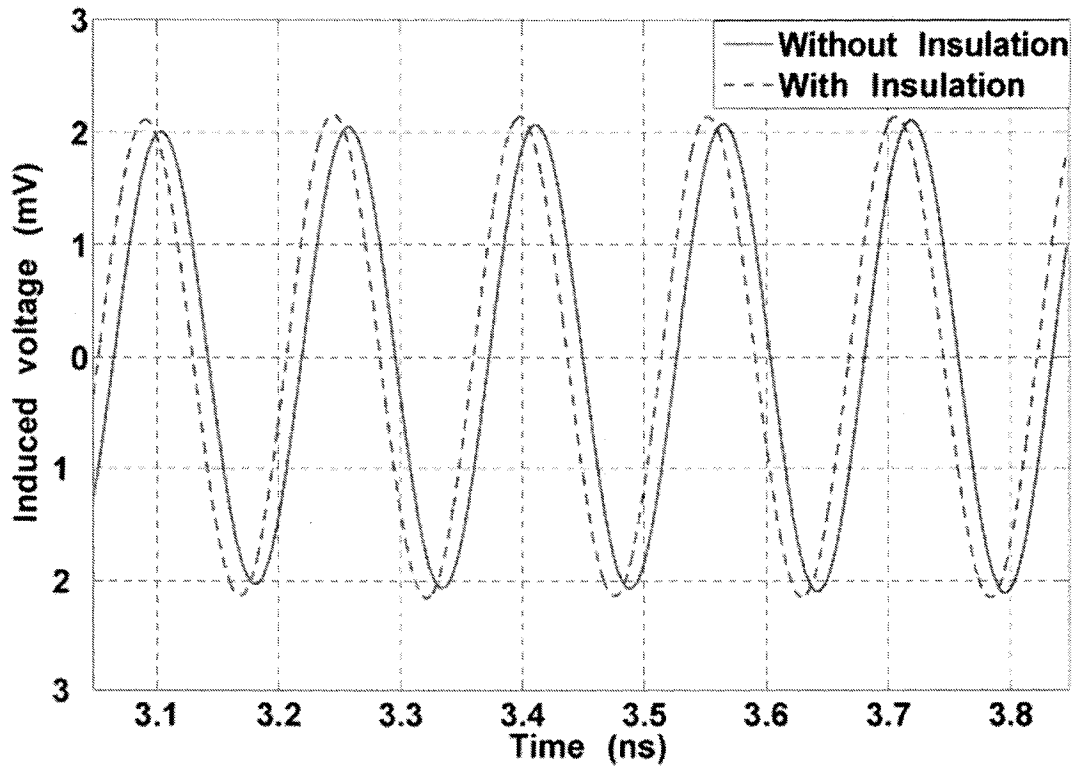


Figure 4.6 Wire dipole antenna with insulation layer. Above: insulated wire dipole shown in the x - y plane; Below: insulated wired dipole cross-section view.

In our simulations, we matched the insulation layer dielectric constant ϵ_{er} with its immediate surrounding environment to minimize wave reflections due to dielectric material discontinuity. This might not be the case in real applications as the manufacturer might use one generic insulation material for devices implanted in different layers of the living tissue to reduce the production cost. The antenna is placed 1.7mm into the skin layer ($z = -1.7\text{mm}$) and it is 2mm to the skin/fat interface. The thickness of the fat layer is 20mm and underneath muscle layer has the proper thickness as discussed earlier. The induced voltage waveforms are shown in Figure 4.7. At both 403.5MHz and 6.5GHz, the induced voltage on the antenna with insulation layer is higher than the one without insulation layer. Similar behavior has been observed when the antenna is embedded in the fat and muscle layers as well. This effect of the insulation layer on the induced open-circuit voltage is more visible when the surrounding tissue media have high conduction loss. An illustration of this point is offered in Figure 4.8, where the induced open-circuit voltages are graphed for excitation at 6.5GHz in the muscle tissue. The same dipole antenna with insulation layer produces an open-circuit voltage about 50% higher than the voltage level of the non-insulated antenna.



(a)



(b)

Figure 4.7 Simulated induced voltage on the dipole antenna with and without insulation layer at (a) 403.5MHz and (b) 6.5GHz.

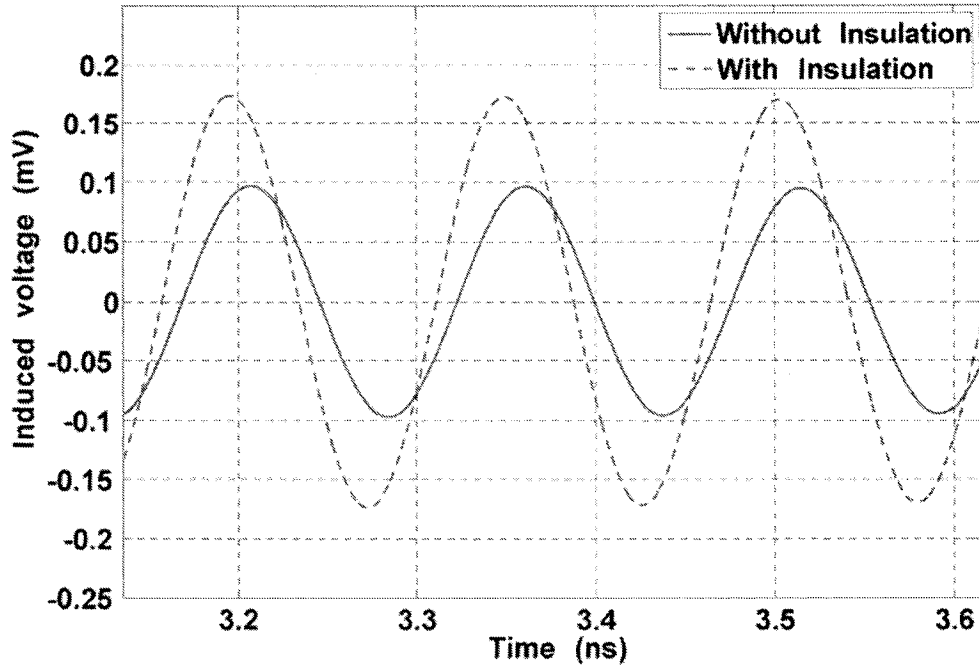


Figure 4.8 Induced voltage on the dipole antenna in muscle layer at 6.5GHz with and without insulation.

4.3.2 The Effect of Fat Layer Thickness

The thickness of fat layer varies considerably among human individuals and with body locations. In this part of the thesis, we study the effect of the fat layer thickness on the induced voltage. The antenna used in this section is the same as the one used shown in Figure 4.5. The antenna is placed 1.7mm into the skin layer ($z = -1.7\text{mm}$) and it is 2mm to the skin/fat interface. The thickness of fat layer varies from 5mm to 10mm to 20mm. The underneath muscle layer is 100mm thick at 403.5MHz and 20mm thick at 6.5GHz. The induced voltage waveforms at 403.5MHz with various fat layer thicknesses are shown in Figure 4.9(a). The simulation results suggest that at 403.5MHz the thicker the fat layer is, the higher voltage induces on the antenna embedded in skin layer. This is due to the fact that the reflection at the skin/fat interface increases with the increase of the fat layer thickness from 5mm to 10mm to 20mm. The electric field magnitude in the skin layer increases accordingly. This is again confirmed by the field calculation using the Matlab script developed earlier. The field is plotted in Figure 4.9(b) showing the tendency of higher electric field magnitude at $z = -1.7\text{mm}$ with thicker fat layer.

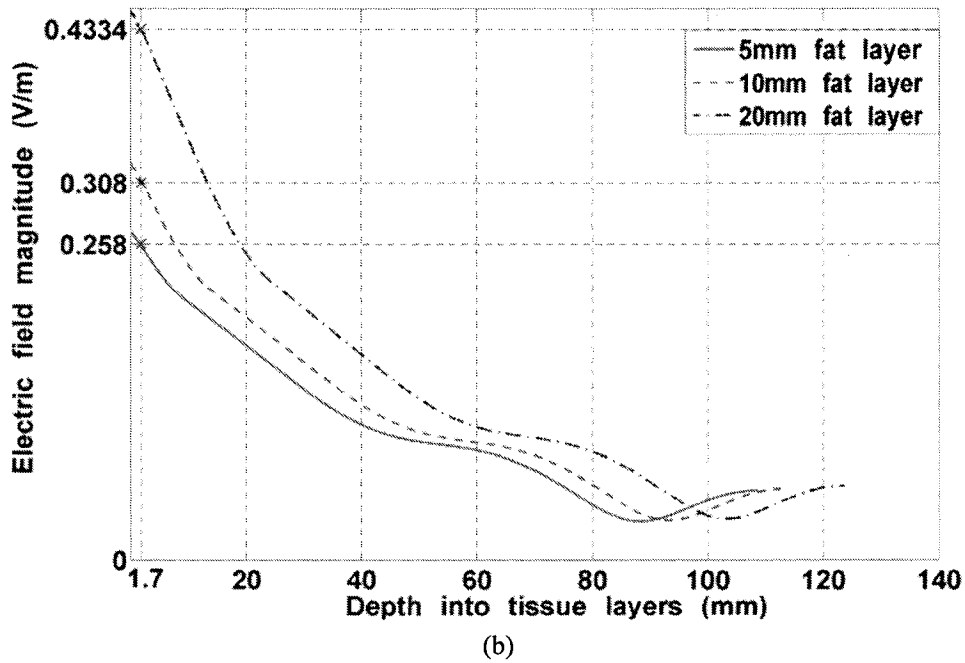
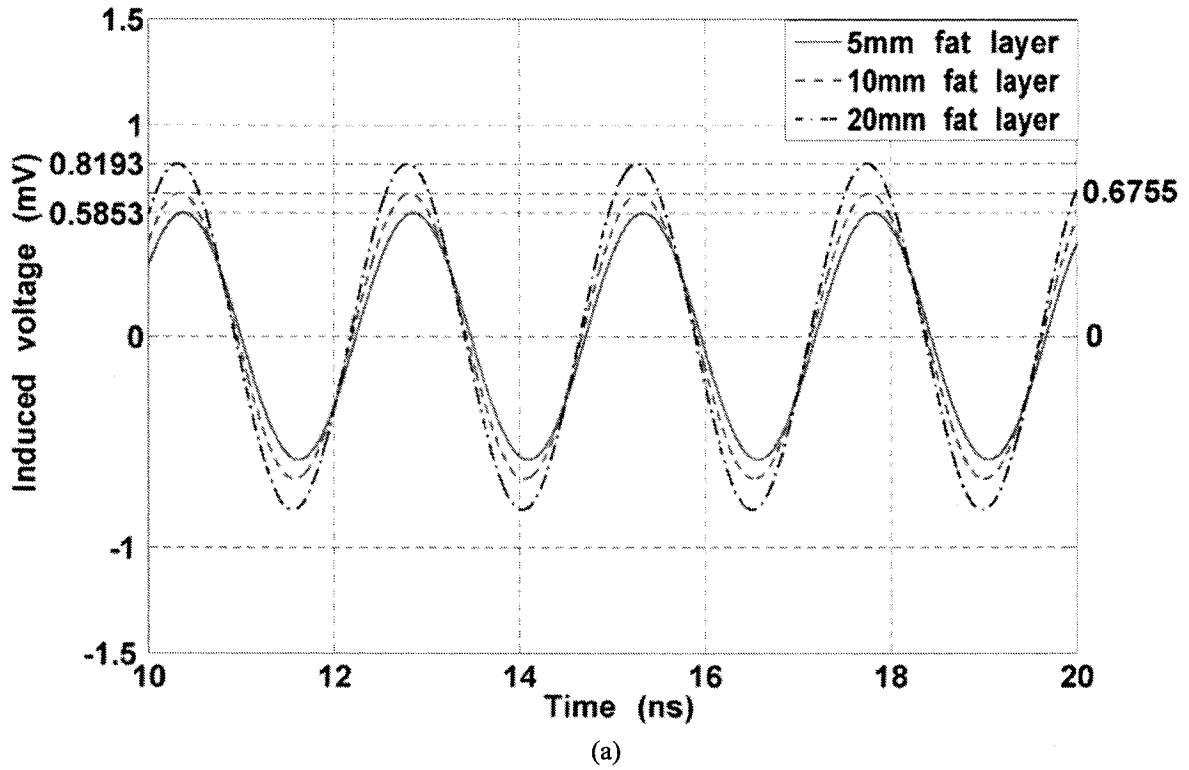
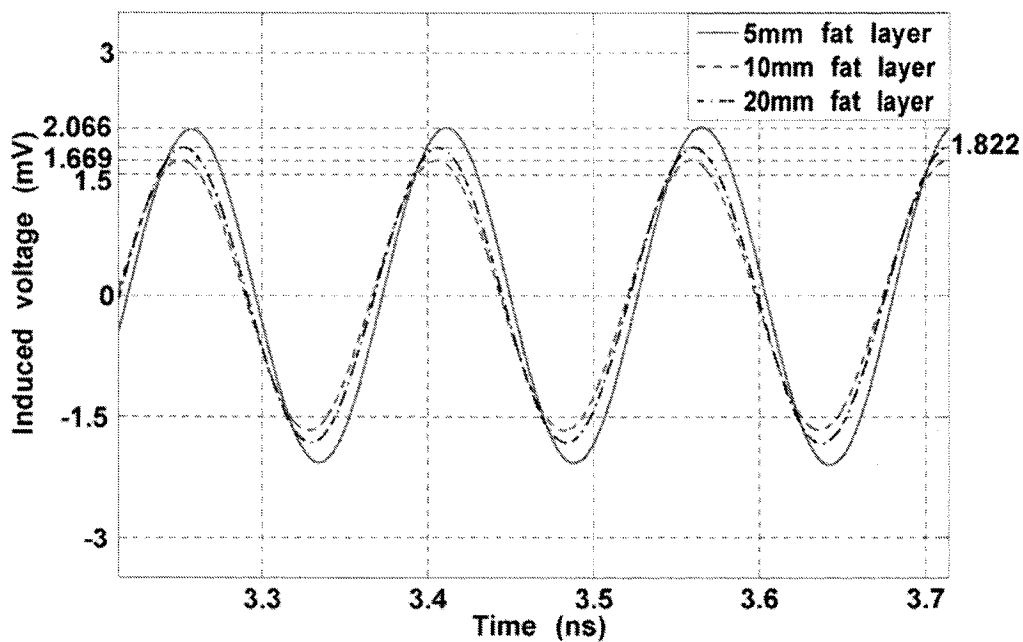


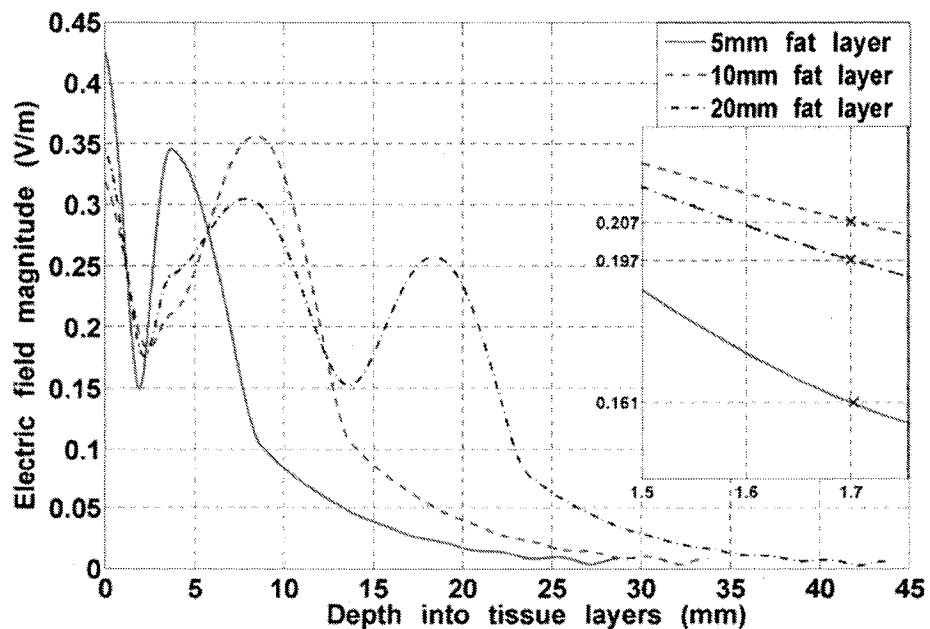
Figure 4.9 Effect of increasing fat layer thickness at 403.5MHz on (a) induced voltage and (b) electric field magnitude.

Induced voltage waveforms at 6.5GHz are shown Figure 4.10(a). Simulation indicates that at 6.5GHz, a 5mm thick fat layer results in the highest induced voltage on the dipole

antenna followed by a 20mm and a 10mm thick fat layer. This result does not suggest a simple increasing or decreasing relation between the thickness of the fat layer and the induced open-circuit voltage. For verification, the subsequently calculated electric field magnitude is shown in Figure 4.10(b).



(a)



(b)

Figure 4.10 Effect of the increasing fat layer thickness at 6.5GHz on (a) induced voltage and (b) electric field magnitude.

Field calculations in Figure 4.10(b) suggest that a 10mm thick fat layer results in the strongest electric field at $z = -1.7\text{mm}$, followed by a 20mm and a 5mm thick fat layer. This does not intuitively relate to the voltage simulation results shown in Figure 4.10(a). The electric fields calculated in Figure 4.10(b) are under the assumption that no scatter field is present. This is clearly not the case when the antenna is embedded. Due to this reason, the calculated electric field magnitude does not suggest the same tendency as the voltage simulated in SEMCAD-X. To clarify this, we use the SEMCAD-X build-in field sensor to monitor the field distribution. This numerical sensor can calculate the field distributions in the presence of the antenna structure. The results are shown in Figure 4.11 and they confirm that, with the scatter fields present, a 5mm thick fat layer results in the strongest electric field at $z = -1.7\text{mm}$ followed by a 20mm and a 10mm thick fat layer. These results are consistent with the induced voltage results shown in Figure 4.10(a).

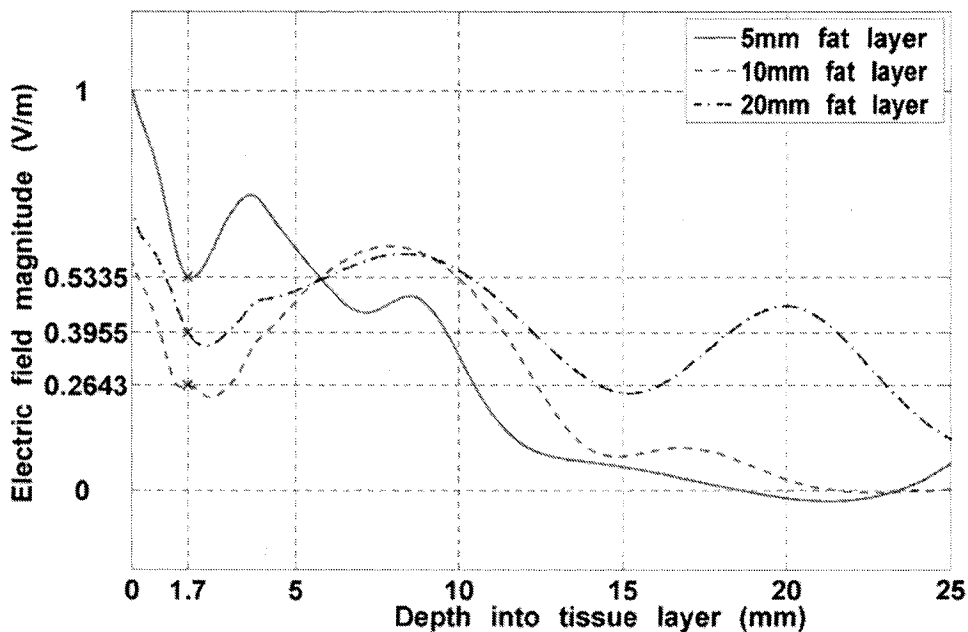
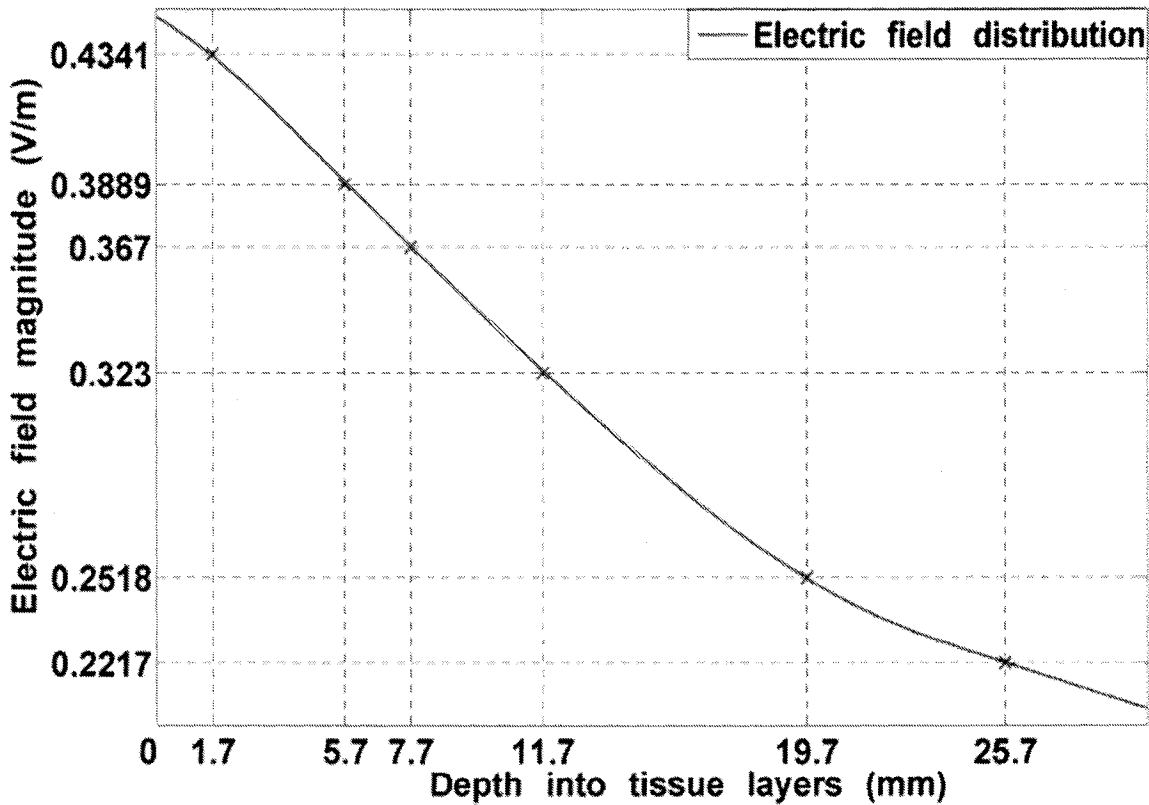


Figure 4.11 Electric field magnitude distribution at 6.5 GHz simulated with SEMCAD-X.

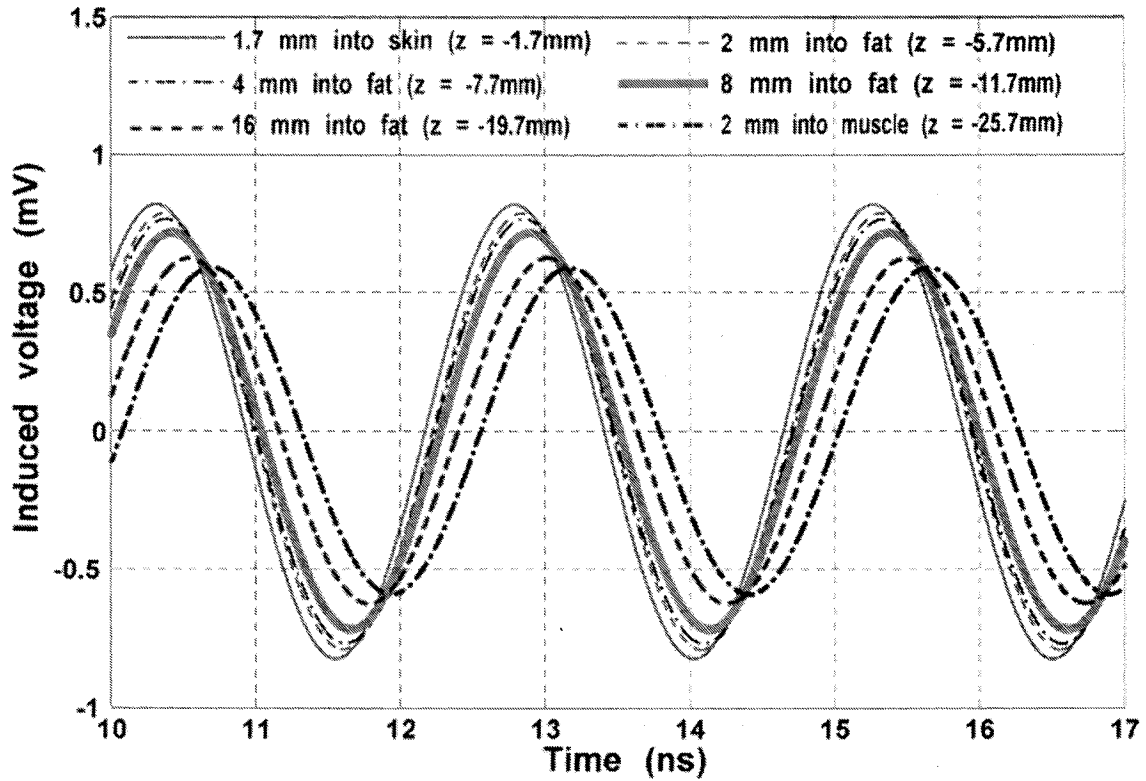
4.3.3 The Effect of Antenna Embedded in Different Tissue Layers

In this section, we place the antenna in different locations in the tissue model. The thickness of the skin and fat layer is 3.7mm and 20mm, respectively. The underlying muscle layer is 100mm thick at 403.5MHz and 20mm thick at 6.5GHz. The antenna used in this section is depicted in Figure 4.5.

As suggested in the previous sections, the induced voltage is highly correlated with the electric field magnitude. At 403.5MHz, the electric field magnitude decreases with the z coordinate (with increase depth into the tissues). This is shown in Figure 4.12(a). The same trend is observed in Figure 4.12(b) as the induced open-circuit voltage drops with the antenna moved progressively deeper into the tissues. At 6.5GHz, the field distribution is more complicated as shown in Figure 4.13(a). Induced voltage waveforms are shown in Figure 4.13(b). Field calculation indicates that the electric field magnitude reaches the maximum at $z = -7.7\text{mm}$ and followed by $z = -5.7\text{mm}$, -19.7mm , -11.7mm , -1.7mm and reaches the minimum at $z = -25.7\text{mm}$. This is consistent with the order of the simulated open-circuit voltages from highest to lowest as shown in Figure 4.13(b). Induced voltages at both frequencies are summarized in Table 4.3.

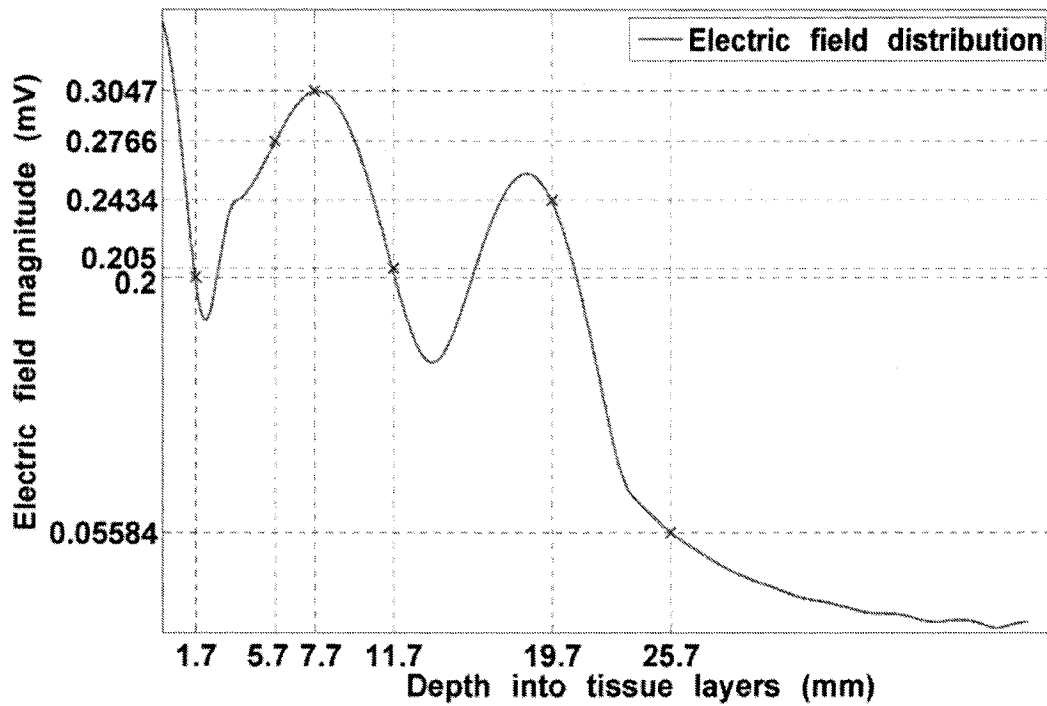


(a)

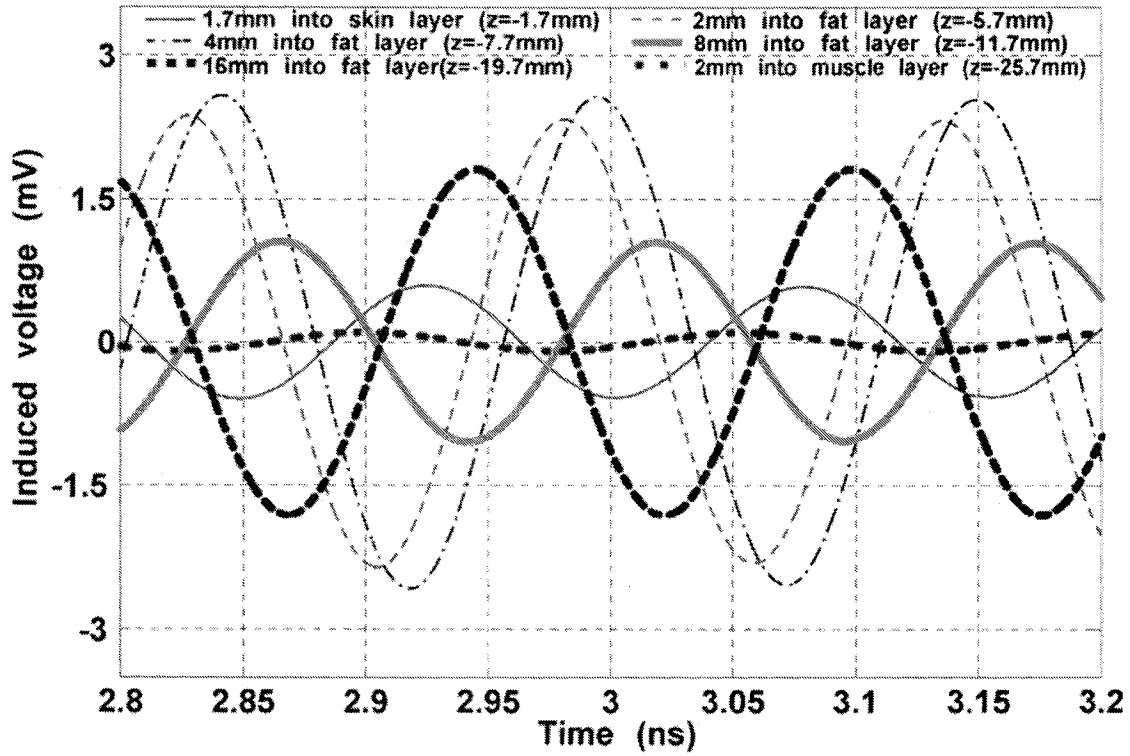


(b)

Figure 4.12 (a) Calculated electric field magnitude and (b) simulated induced voltage waveforms at various locations at 403.5MHz.



(a)



(b)

Figure 4.13 (a) Calculated electric field magnitude and (b) simulated induced voltage waveforms at various locations at 6.5GHz.

Table 4.3 Simulated induced peak voltages at various locations at 403.5MHz and 6.5GHz.

Tissue	Implant locations	Induced peak voltage	
		403.5 MHz	6.5 GHz
Skin	1.7mm to air/skin interface (z = -1.7mm)	0.8201 mV	0.5773 mV
Fat	2mm into fat (z = -5.7mm)	0.7878 mV	2.334 mV
	4mm into fat (z = -7.7mm)	0.7666 mV	2.566 mV
	8mm into fat (z = -11.7mm)	0.7156 mV	1.045 mV
	16mm into fat (z = -19.7mm)	0.6236 mV	1.811 mV
Muscle	2mm into muscle (z = -25.7mm)	0.5882 mV	0.09822 mV

4.3.4 Dipole Antenna with Different Length

In this section, we simulate two dipole antennas with different length. The long dipole (original size dipole) is 53mm in length and the short dipole (scaled 1/10th of the original) is 5.3mm in length as shown in Figure 4.5. The antennas are placed 1.7mm into the skin

layer ($z = -1.7\text{mm}$). The thickness of the skin layer and the fat layer is 3.7mm and 20mm respectively. The underlying muscle layer is 100mm at 403.5MHz and 20mm at 6.5GHz . Induced voltage waveforms are shown in Figure 4.14. At 403.5MHz , the induced voltage on the original dipole is higher than the scaled dipole. At 6.5GHz , voltage induced on the scaled dipole is higher than the original dipole, as the scaled dipole embedded in skin tissue behaves as a half-wave resonant dipole around 6.5GHz .

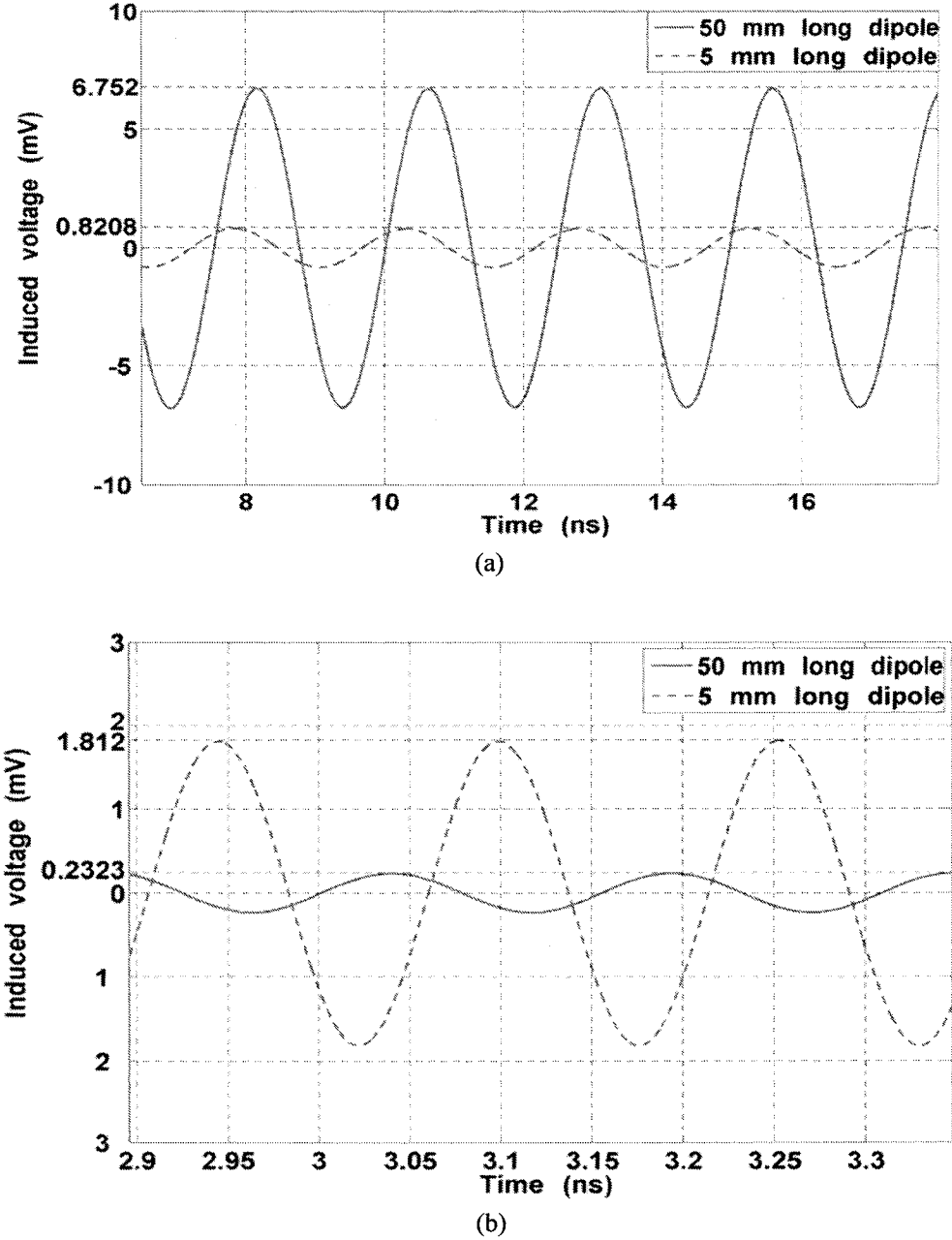


Figure 4.14 Simulated induced voltage on the open terminals of the 53mm-long dipole and 5.3mm-long dipole at (a) 403.5MHz and (b) 6.5GHz .

4.4 Spiral Antenna

A set of studies parallel to those outlined for the dipole antenna are carried out for a spiral antenna. The results, practically identical, are omitted here in the interest of saving space, with the note that they bring us to the conclusions previously drawn for the dipole antenna. In this section, we use the features of the spiral antenna to discuss the effect of polarization of the impinging waves on the induced voltage at the antenna terminals.

4.4.1 Effect of Incident Wave Polarization

Unlike the linearly polarized wire dipole antenna, polarization of spiral antenna is a function of frequency. In this part of thesis, we observe polarization mis-match for the spiral antenna at 403.5MHz and 6.5GHz. The geometry and dimension of the spiral antenna are shown in Figure 4.15. The spiral antenna is modeled to be 70 μ m thick.

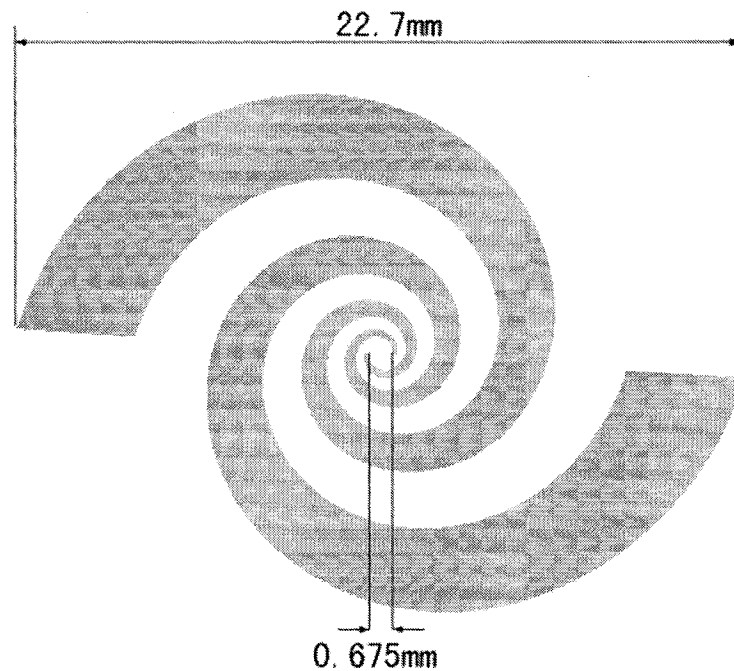
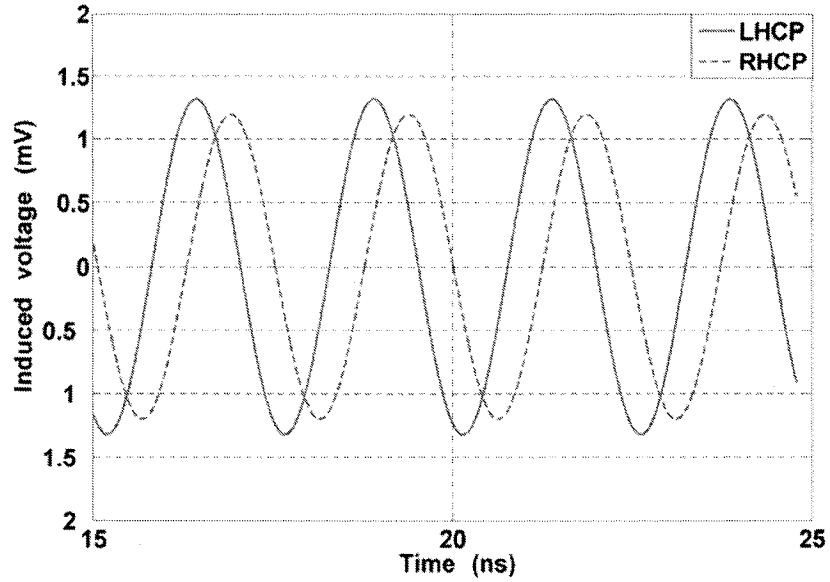


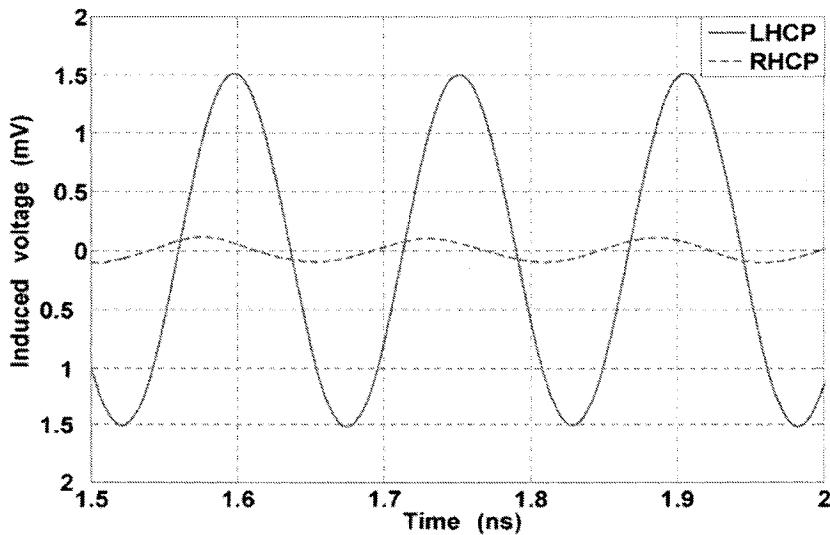
Figure 4.15 Geometry and dimension of the spiral antenna. The antenna is modeled to be 70 μ m thick.

At both frequencies, this spiral antenna is placed 1.7mm into the skin layer ($z = -1.7$ mm). The thickness for relevant tissue layers are: 3.7mm for the skin layer, and 20mm for the fat layer. The muscle layer is 100mm at 403.5MHz and 20mm at 6.5GHz. The plane-wave polarization was altered between Left Hand Circular Polarization (LHCP) and Right Hand

Circular Polarization (RHCP) at both frequencies. To generate these circularly polarized plane-waves in SEMCAD-X, two overlapped plane-wave sources are used. One of the sources is linearly polarized in horizontal direction (x -direction) and the other one is linearly polarized in vertical direction (y -direction). The two sources are out of phase by 0.25 periods for RHCP and 0.75 periods for LHCP. The complete field is a $-z$ propagated circularly polarized plane-wave. The induced voltages on the spiral antenna with various polarizations are shown in Figure 4.16.



(a)



(b)

Figure 4.16 Simulated induced voltage waveforms with a LHCP plane-wave and a RHCP plane-wave for two frequencies of interest: (a) 403.5MHz and (b) 6.5GHz.

At 403.5MHz, the spiral antenna is linearly polarized, therefore, the wave reception resulted in approximately the same level of voltage from either RHCP incoming plane-wave or LHCP incoming plane-wave. However, at 6.5GHz, the spiral antenna itself is circularly polarized, therefore, the induced voltages are significantly different between the RHCP incoming wave and LHCP incoming wave. Figure 4.16(b) suggests that this spiral antenna is LHCP at this frequency.

4.5 Impedance Consideration – Dipole and Spiral Antenna

For maximum power transfer, the impedance of the antenna must match with the impedance of the rectifier in the next stage in a complex conjugate manner. In this section, we excite the antenna structure with an edge source and simulate the feed point impedance. Due to the broadband nature of this group of simulations, the dispersive characteristics of the tissue materials must be taken into account. In section 4.5.1, we discuss how the dispersive material can be implemented in SEMCAD-X and in section 4.5.2 we show the simulated impedance results.

4.5.1 Cole-Cole to Debye model Conversion for Dispersive material

Due to the time-domain nature, FDTD scheme cannot handle the multi-term Cole-Cole expression (Equation 2.18) with ease. This difficulty originates largely from the fact that the empirical distribution parameter α_n is introduced as a fraction number in the exponent. This fractional exponent translates itself into time domain as the solver needs to access field data at unavailable time instance that is in-between the integer time steps of the FDTD scheme. Therefore, SEMCAD-X does not support Cole-Cole model directly for the dispersive material. Unfortunately, most of the parameters found to model dispersive tissue media are for the Cole-Cole model [20]. Therefore, a mathematical conversion from the Cole-Cole model to the Debye model (Equation 2.17) is necessary if a broadband simulation involving dispersive material is needed. An algorithm developed in [37] accomplishes this conversion by using Minimum Square Error (MSE) curve fitting technique. MSE is applied to fit a Debye model to the data points calculated using the Cole-Cole model. A Matlab implementation of this algorithm is developed and presented in

Appendix C. A three-pole Debye model is used to curve fit the imaginary part of the complex permittivity from 1GHz to 100GHz. The real part of the complex permittivity is then automatically fit with the model. As an example shown in Figure 4.17, relative permittivity and conductivity of the fat tissue is calculated using both the Debye model and the Cole-Cole model and plotted on logarithmic scale from 1GHz to 100GHz. The two curves match very well over the broadband frequency range. The Debye model parameters for the skin, fat and muscle tissues are shown in Table 4.4. These parameters are used in Equation 2.17 (with $n = 3$) to calculate the relative permittivity and conductivity of the corresponding tissues.

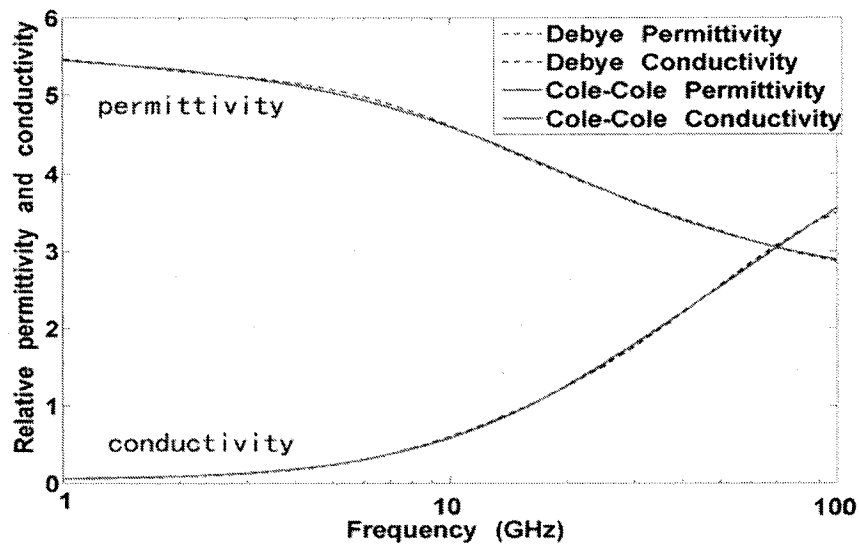


Figure 4.17 Relative permittivity and conductivity of fat calculated using Cole-Cole model and Debye model.

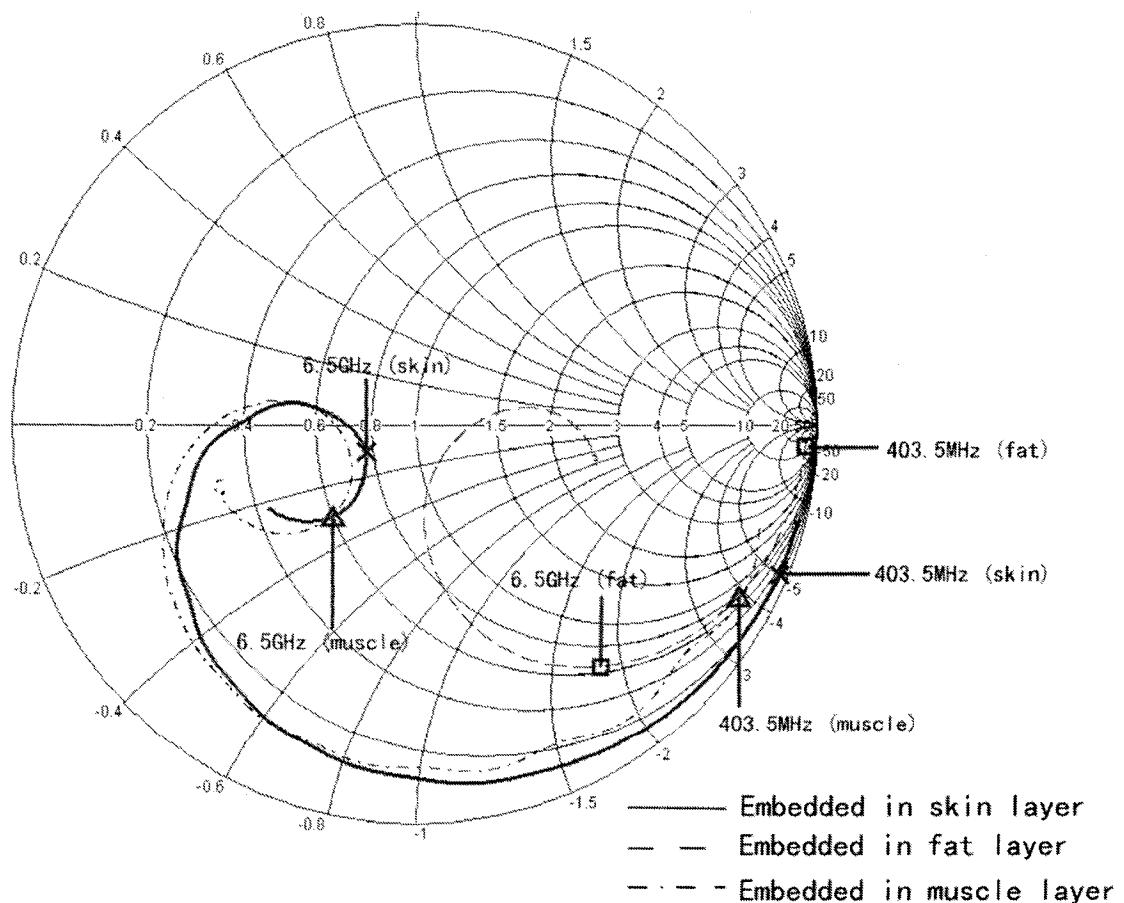
Table 4.4. Debye parameters used to model tissue materials.

Tissue	Relaxation time (ns)	Weight
Skin	$\tau_1 = 0.07958$	$A_1 = 1.8870$
	$\tau_2 = 0.00114$	$A_2 = 0.6759$
	$\tau_3 = 0.00035$	$A_3 = 0.3121$
Fat	$\tau_1 = 0.7958$	$A_1 = 1.4628$
	$\tau_2 = 0.0133$	$A_2 = 0.5332$
	$\tau_3 = 0.0032$	$A_3 = 0.3599$
Muscle	$\tau_1 = 0.01592$	$A_1 = 3.1676$
	$\tau_2 = 0.0001$	$A_2 = 0.6695$
	$\tau_3 = 0.00003$	$A_3 = 0.2965$

4.5.2 Impedance of Dipole and Spiral Antenna

In this section, we present the simulated impedances for the dipole antenna and the spiral antenna when they are embedded in different tissue layers. The two antennas have the same dimension and geometry as shown in Figure 4.5 and Figure 4.15 respectively. The impedances are shown on the Smith chart with normalization to $50\ \Omega$. The markers indicate the impedances at both 403.5MHz and 6.5GHz. The results are shown in Figure 4.18 and numerical summaries are shown in Table 4.5.

As the Smith chart suggests, the 5mm-long dipole in muscle or skin layer is relatively easy to match at 6.5GHz as it behaves as a resonant half-wave dipole around this frequency. Spiral antenna is much more difficult to match, especially at 403.5MHz. We also notice that, without insulation layer, the spiral no longer operates as a frequency independent antenna in the lossy dielectric media.



(a)

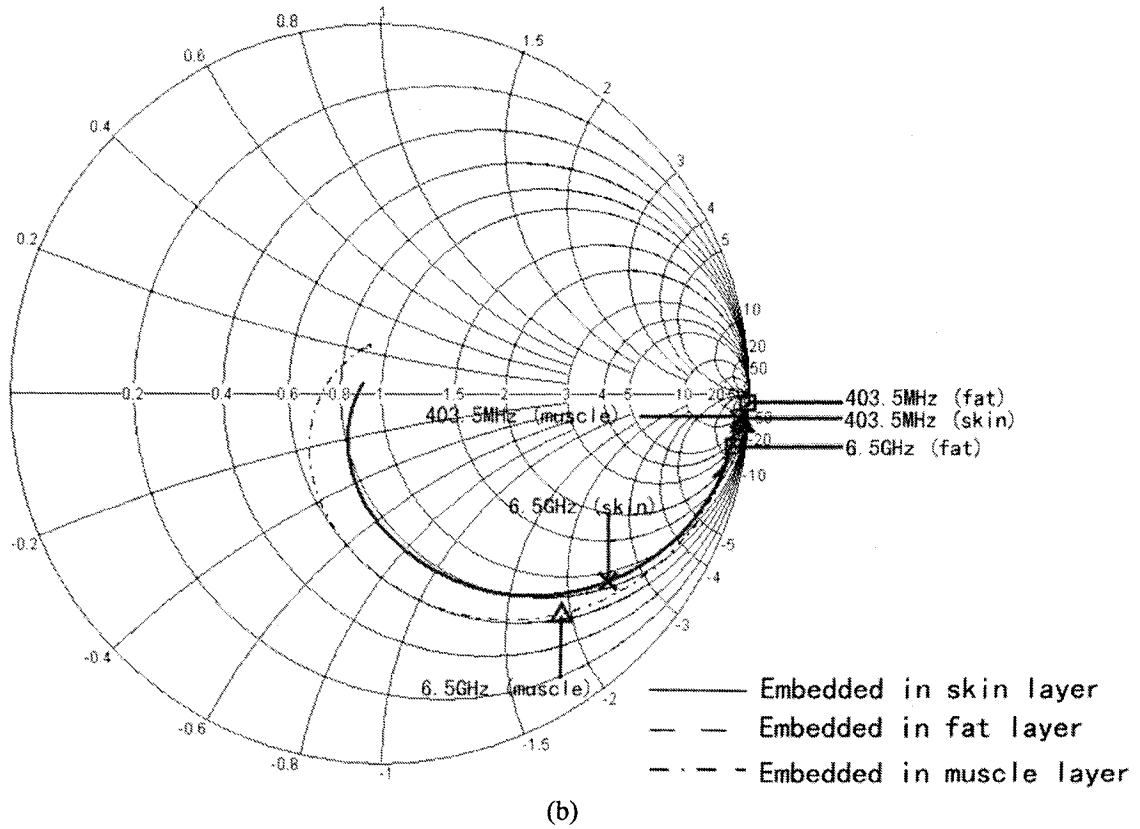


Figure 4.18 Simulated impedance of (a) wire dipole antenna and (b) spiral antenna at both 403.5MHz and 6.5GHz.

Table 4.5 Summary of the impedance values for dipole and spiral antenna at 403.5MHz and 6.5GHz.

Dipole embedded location	Impedance (normalized with respect to $50\ \Omega$)	
	403.5MHz	6.5GHz
(z = -1.7mm) Skin	0.319-j5.001	0.77-j0.153
(z = -7.7mm) Fat	14.311-j26.163	0.658-j1.824
(z = -25.7mm) Muscle	0.675-j3.738	0.5999-j0.301

Spiral embedded location	Impedance (normalized with respect to $50\ \Omega$)	
	403.5MHz	6.5GHz
(z = -1.7mm) Skin	11.833-j25.953	0.897-j2.378
(z = -7.7mm) Fat	115.19-j212.782	4.248-j20.277
(z = -25.7mm) Muscle	12.765-j22.31	0.665-j1.923

Chapter 5

Conclusions and Directions for Future Work

In this work, we studied the possibility of utilizing an antenna as part of the rectifier-antenna system to power up implants for bio-telemetry applications. To design such system, it is important to study the behaviour of antennas when embedded in biological tissues. In particular to this thesis, we studied the induced open-circuit voltage when the antenna was embedded in different locations in a layered-tissue model and illuminated by a plane-wave.

We first built the classic three-layer tissue model in SEMCAD-X, electromagnetic simulation tool based on the finite-difference time-domain method. To complete this layered tissue model, we then verified the necessary muscle layer thickness which would be sufficient to yield negligible reflections from the muscle/air interface (model boundary) through the propagation loss mechanism. Finally, we determined that at our chosen frequencies, it was unnecessary to resolve the skin tissue beyond its single-layer model with dielectric constants that combines, in an average-sense, the dielectric constants of individual thinner layers.

Next, a simple wire dipole antenna and a spiral antenna were embedded and illuminated with a plane-wave. Each of the two antennas had two versions with different physical sizes. All four antennas were simulated with and without an insulation layer at both 403.5MHz and 6.5GHz. In total, we simulated 16 groups of antennas and for each group, the antenna was placed at various locations in the tissue model. A linearly polarized 1V/m plane-wave was used to illuminate the structure and the induced terminal voltage was observed for all cases. From the observed results, we conclude the following:

- At 403.5MHz, the magnitude of electric field is a decreasing function as the depth into tissues increases. Therefore, as expected, the induced voltage drops when the antenna is placed deeper and deeper into the tissue layers. Another observation at this frequency indicates that within our fat layer thickness range [5mm-20mm], induced open-circuit voltage on a skin-layer-embedded antenna terminals increases when the thickness of underneath fat layer increases;

- At 6.5GHz, the electric field distribution is very sensitive to the location (depth) where the observation is made. From a practical point of view, this high sensitivity might be problematic because very little variation in the location could cause significant change of the induced voltage on the antenna terminals;
- For the wire dipole antenna, the highest induced voltage resulted from the original size dipole (53mm-long) at 403.5MHz. However, if limited by physical size to the short dipole (5.3mm-dipole), the maximum induced voltage happens at 6.5GHz. For spiral antenna, the general conclusion follows the same pattern as the dipole antenna;
- For all the cases, using an insulation layer has a desirable effect on the induced open-circuit voltage at both frequencies, in the sense of increased induced terminal voltage with respect to the case of no insulation. As expected, this effect is more notable when the antenna is placed in a very lossy material.

The work presented in this thesis has demonstrated the potential and limitations of using an antenna to receive RF energy when embedded in biological (tissue) complex media. From the simulations, we can estimate that power received by one single antenna is not sufficient to power up existing implanted devices. Further, we suggest the following directions for future studies:

- Design of novel miniaturized broadband antenna structure that can be easily matched at 403.5MHz in a biologically embedded environment;
- Identification of difficulties and related strategies when the incident wave is randomly polarized and/or from a randomly-incident angle;
- Design an antenna array instead of a single antenna element to collect the impinging wave. This strategy is clearly linked to the first suggestion, as the size of the antenna element within the array needs to be further decreased.

Utilizing a miniaturized implanted antenna to receive RF energy to power up a bio-telemetry system is a novel technique still at its infant stage. We hope that our work will contribute to the future development of systems that can effectively replace the usage of batteries and cables in the bio-telemetry systems, allowing for advanced research in neurophysiology and the consequent applications.

References

- [1] Negar Tavassolian, “Imaging Breast Tumors with Microwaves: Simulation-Based Assessment of Detection Capabilities of a Broadband Antenna-Sensor”, Master Thesis, August 2004.
- [2] Jaehoon Kim, Yahya Rahmat-Samii, “Implanted Antennas Inside a Human Body: Simulations, Designs, and Characterizations”, *IEEE Transactions on Microwave Theory and Technique*, vol. 51, pp. 1934–1943, August 2004.
- [3] N.H. Ismail, H.D. Ramadan, “Radiation of electromagnetic waves by a circular phased aperture antenna for neck hyperthermia”, *Radio Science Conference, 2001. NRSC 2001. Proceedings of the Eighteenth National*, vol. 2, pp. 653-660, March 2001.
- [4] Jaehoon Kim, Yahya Rahmat-Samii, “An Implanted Antenna in the Spherical Human Head: SAR and Communication Link Performance”, *IEEE Topical Conference on Wireless Communication Technology*, 2003.
- [5] R.N. Simons, D.G. Hall, F.A. Miranda, “RF Telemetry System for an Implantable Bio-MEMS Sensor”, *Microwave Symposium Digest, 2004 IEEE MTT-S International*, vol. 3, pp. 1433- 1436, June 2004.
- [6] Frank Carden, *Telemetry Systems Design*, Artech House 1995.
- [7] Frank Carden, Russell Jedlicka, Robert Henry, *Telemetry Systems Engineering*, Artech House 2002.
- [8] Mackay R.S., *Bio-Medical Telemetry: Sensing and Transmitting Biological Information from Animals and Man*, IEEE Press 1993.
- [9] Thomas F. Budinger, “Biomonitoring with wireless communications”, *Annu Rev Biomed Eng*, 5:383-412, 2003.
- [10] Iddan G, Meron G, Glukhovskiy A, Paul Swain, “Wireless capsule endoscopy”, *Nature* Vol.405 pp.40-417, May 2000.
- [11] RF SYSTEM website at <http://www.rfamerica.com/>
- [12] Yahya Rahmat-Samii and Jaehoon Kim, *Implanted Antennas in Medical Wireless Communications*, Morgan & Claypool Publishers, June 2006.
- [13] L. Li, P. Kooi, M. Leong, and T. Yeo, “Electromagnetic dyadic Green’s function in spherically multilayered media” *IEEE Transactions on Microwave Theory and Technique*, vol. 42, no. 12, pp. 2302–2310, Dec. 1994.

- [14] C. T. Tai, *Dyadic Green's Functions in Electromagnetic Theory*, Scranton, PA: Intext Education, 1971.
- [15] K.S. Lee, "Numerical solution of initial boundary value problems involving Maxwell's equations in isotropic media," *IEEE Transactions on Antennas and Propagation*, vol. 14, no.3, pp. 302-307, May 1966.
- [16] D.M. Sullivan, *Electromagnetic Simulation Using the FDTD method*, IEEE Press Series on RF and Microwave Technology, 2000.
- [17] Semcad Website: <http://www.semcad.com>, 2007.
- [18] Andres J Johansson, *Wireless Communication with Medical Implants - Antennas and Propagation*, Ph.D dissertation.
- [19] FCC Website:
http://wireless.fcc.gov/services/index.htm?job=service_home&id=medical_implant
- [20] C Gabriel et al, "The dielectric properties of biological tissues: III. Parametric models for the dielectric spectrum of tissues", *Phys Med Biol*. Vol.41 Issue 11, pp.2271-2293. 1996 Nov.
- [21] William G. Scanlon, J. Brian Burns, and Noel E. Evans, "Radiowave Propagation from a Tissue Implanted Source at 418 MHz and 916.5 MHz", *IEEE Transaction on Biomedical Engineering*, vol.47, no.4, pp527-534, April 2000.
- [22] Ronold King, Sheila Prasad, Barbara Sandler, "Transponder Antennas In and Near a Three-Layered Body", *IEEE Transactions on Microwave Theory and Technique*, vol.28, no.6, pp.586-596, June 1980.
- [23] R.M.Marks, S.P. Barton, C.Edwards, *The Physical Nature of the Skin*, MTP Press, 1988.
- [24] Foster and Schwan, "Dielectric properties of tissues and biological materials: a critical review", *Crit.Rev. Biomed. Eng.* 17 25-104.
- [25] William D. Hurt, "Multiterm Debye Dispersion Relations for Permittivity of Muscle", *IEEE Transaction on BioMedical Engineering*, vol. 32, no.1, pp60-64, January 1985.
- [26] Italian National Research Council, Institute for Applied Physics, Dielectric Properties of Body Tissue project website at
<http://niremf.ifac.cnr.it/tissprop/htmlclie/htmlclie.htm>.
- [27] Joseph A. Hagerty, B. Helmbrecht, William H. McCalpin, Regan Zane and Zoya B. Popović, "Recycling Ambient Microwave Energy With Broad-Band Rectenna Arrays", *IEEE Transactions on Microwave Theory and Technique*, vol.52, no.3, pp.1014-1024, March 2004.

- [28] Constantine A. Balanis, *Antenna Theory – Analysis and Design*, Chapter 11, John Wiley & Sons, Inc.
- [29] Houssam Kanj, Yi Zhang and Milica Popović, “Advantage of Modeling Broadband Antennas with “SENCAD X” FDTD Conformal Solver”, accepted for ACES 2007 Conference, Verona, Italy, April 2007.
- [30] Florian B. Helmbrecht, “A Broadband Rectenna Array for RF Energy Recycling”, Diplom-Ingenieur (TU-München) thesis, September 2002.
- [31] Joseph A. Hagerty, Branko D. Popović and Zoya B. Popović, “Broadband Rectenna Arrays for Randomly Polarized Incident Waves”, 30th European Microwave Conference, pp. 13-16, 2000.
- [32] United States Frequency Allocation: <http://www.ntia.doc.gov/osmhome/allochrt.pdf>
- [33] IEEE Std C95.1, 1999 Edition: IEEE Standard for Safety Levels with Respect to Human Exposure to Radio Frequency Electromagnetic Fields, 3 kHz to 300 GHz, IEEE, New York, NY, 1999.
- [34] FCC OET Bulletin 65 Edition 97-01: Evaluating Compliance with FCC Guidelines for Human Exposure to Radiofrequency Electromagnetic Fields, FCC, Washington D.C., 1997.
- [35] ICNIRP Guidelines: Guidelines for Limiting Exposure to Time-Varying Electric, Magnetic, and Electromagnetic Fields (up to 300 GHz), *Health Physics*, vol. 74, no. 4, pp. 494-522, 1998.
- [36] Centre of biomedical Technology and Physics, Medical University Vienna
<http://www.meduniwien.ac.at/zbmtp/bmt/home.htm>.
- [37] David F. Kelley and Raymond J. Luebbers, “Debye Function Expansions of Empirical Models of Complex Permittivity for Use in FDTD Solutions”, IEEE Antennas and Propagation Society International Symposium, 2003. IEEE Publication vol. 4, pp. 372-375, June 2003

Appendix A

Related Publications

- H. Kanj, Y. Zhang and M. Popovic, " **Advantage of Modeling Broadband Antennas with "SENCAD X" FDTD Conformal Solver** ", ACES 2007 Conference, Verona, Italy, April 2007

Advantage of Modeling Broadband Antennas with “SENCAD X” FDTD Conformal Solver

Houssam Kanj, Yi Zhang and Milica Popović

Department of Electrical and Computer Engineering
McGill University, Montreal Quebec, Canada
hkanj@po-box.mcgill.ca, yi.zhang5@mail.mcgill.ca, milica.popovich@mcgill.ca

Abstract: This paper presents an assessment study of the accuracy and speed of modeling a curved broadband structure with the finite-difference time-domain (FDTD) conformal solver in “SEMCAD X”. In particular, the test structure is a disk dipole antenna, chosen for its simplicity, symmetry and curved boundaries which best differentiate and compare results of the conformal and the standard staircase FDTD solvers. The disk dipole was first simulated with the finite-element software (HFSS). Simulation results confirmed that the conformal model provided significant improvement over the staircase version even when using a very coarse spatial resolution.

Keywords: finite elements, standard FDTD, conformal FDTD, disk dipole

1. Geometry of the Model

Disk dipole antenna was first proposed in 1994 [1]. The curved boundaries of the antenna motivated our choice to use it as a test case for the conformal versus the staircase FDTD solvers. In addition, disk dipole antenna exhibits broadband behavior [2] which enables us to compare the different solvers over a broad frequency range. Figure 1 shows the antenna structure used in our study and its orientation relative to the coordinate axes. The radius of each disk is 15 mm and the antenna is 70 μm thick (in the z-direction). The 1 mm spacing between disks (in the x-direction) accommodates for the feed. The antenna was analyzed in free space.

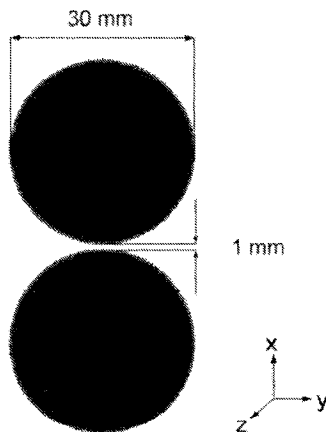


Fig. 1. Geometry, dimensions and the orientation of the disk dipole antenna used in the study.

2. Finite-Element Simulation

The disk dipole antenna described in the previous section was initially simulated in HFSS [3]. HFSS is based on a full-wave finite-element method (FEM), intrinsically conformal in its mesh generation. Two types of metallic materials were used for simulations: copper, with electric conductivity $\sigma_{\text{Cu}} = 5.8 \times 10^7$ S/m and relative permeability $\mu_{\text{r-Cu}} = 0.999991$ and the perfect electric conductor (PEC). The feed structure was modeled as a lump port on a rectangular section of size $0.07 \text{ mm} \times 1 \text{ mm}$. A radiation boundary was constructed on the surfaces of a large free-space box containing the disk dipole antenna. The structure was analyzed at 12 GHz with a frequency sweep from 0.5 GHz – 12 GHz. Two metallic types yield nearly identical return loss S_{11} results as graphed in Figure 2. This outcome is expected due to very small conduction loss of copper in the specified frequency range. Next, we simulated the same structure with the FDTD software using the conformal and standard FDTD methods and compared the results with HFSS PEC as the reference.

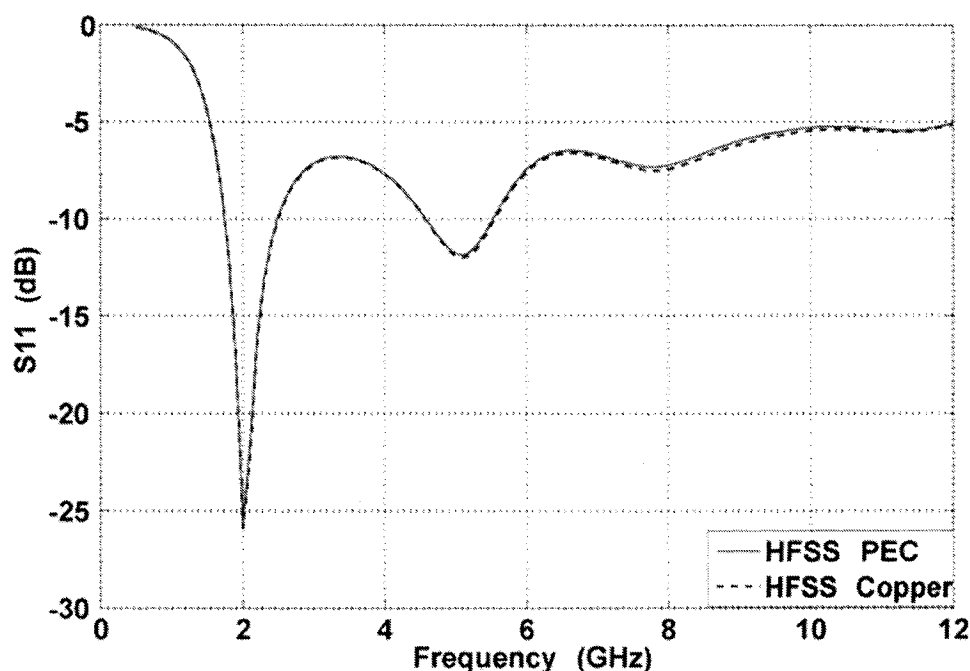


Fig. 2. Finite-element method results (HFSS): Return loss of the antenna in Figure 1 modeled as perfect electric conductor (PEC) or as copper, with $\sigma_{\text{Cu}} = 5.8 \times 10^7$ S/m and relative permeability $\mu_{\text{r-Cu}} = 0.999991$.

3. Simulations in SEMCAD

SEMCAD is a full-wave simulation tool that deploys the FDTD method [4]. The source model does not necessitate actual physical port but is defined by the terminal line only. Two grid-generating schemes are available: (1) the conformal solver (CFDTD) and (2) the staircase grid generator for the standard solver (FDTD). The conformal solver, as the name suggests, follows the curved portion of the model closely by introducing changes to the appropriate FDTD coefficients [5], in contrast to the staircase mesh, which approximates the curve by following it in a step-like manner but only in the direction of the main coordinates. Figure 3 illustrates the boundary of the antenna of Figure 1 meshed using the conformal (Figure 3(a)) and the staircase (Figure 3(b)) technique. In each case, the grid generation is controlled by adjusting the maximum step size in each of the three dimensions of the coordinate system.

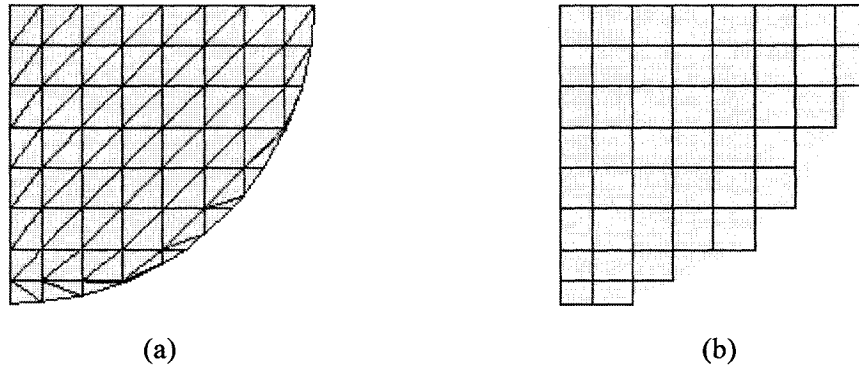


Fig. 3. SEMCAD model of antenna in Figure 1: a sample of a curved antenna edge modeled using (a) the conformal and (b) the staircase grid. Both schemes were tested with the antenna modeled as a perfect electric conductor (PEC)

4. Results and Discussion

To study the effects of different schemes, we simulated the structure using the conformal and the staircase grid. The test cases, with the relevant grid and computing information, are summarized in Table 1. It should be noted that the discretization in the antenna region and the free space region were treated differently. The free space region has the same spatial resolution setup in all cases (in both x - and y -direction) as follows: maximum step 2 mm while the minimum step is defined by the minimum step size in the antenna region. In antenna region the maximum step size is adjusted to generate dense and coarse grids while the minimum step size in antenna region is computed automatically by SEMCAD and reported accordingly in Table 1. For all regions, in z -direction, the minimum step is set to 0.035 mm and the maximum to 2 mm.

With reference to Table 1, we report the following results for the SEMCAD computation of the return loss of the disk antenna depicted in Figure 1.

Figure 4 compares SEMCAD fine (dense) staircase grid results with the results obtained by HFSS. We note a ~ 1 dB difference exists between the SEMCAD and HFSS simulations for the frequency range 2 GHz – 12 GHz.

Figure 5 compares SEMCAD fine (dense) conformal grid results with the results obtained by HFSS. In this case, we note a ~ 0.3 dB difference exists between SEMCAD and HFSS simulation for the frequency range of interest. In subsequent graphs, we will therefore refer to the results for the dense conformal grid as our reference SEMCAD computation of the return loss.

Figure 6 shows that using the same (coarse) grid density, SEMCAD conformal scheme recovers the solution with less than ~ 2 dB difference compared to HFSS over the frequency range of interest. In contrast, staircase scheme has a progressively increased error of more than 5 dB.

Finally, we note in Table 1, that for the same mesh density, the conformal model requires about twice the computational time of that needed for the staircase simulation. This is because we have chosen the highest predefined accuracy option for the conformal solver which translates into one-half of the time-step ($0.5\Delta t$) required by the Courant stability condition (50% CFL). However, it is important to note here that the CFDTD solver available in “SEMCAD X” is stable even when using the conventional stability criteria without any time step reduction, and a time step reduction of $0.7\Delta t$ (70% CFL) is enough to produce highly accurate results [5]. The simulation results are presented in figure 7 where return loss of the disk antenna with time step reduction of $1\Delta t$, $0.7\Delta t$ and $0.5\Delta t$ are shown. As we can see that if time step is chosen to be $1\Delta t$ (i.e. no time reduction) instead of $0.5\Delta t$ as predefined high accuracy in SEMCAD, the total simulation process is speed up by a factor of 2 with only a slightly degrade of accuracy about 0.5 dB.

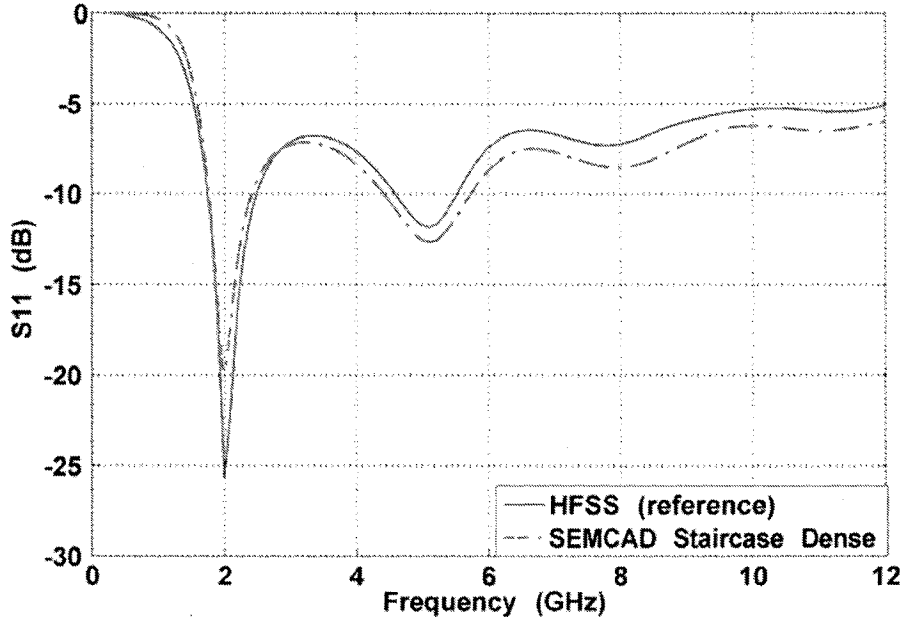


Fig. 4. SEMCAD result for the return loss computed with the dense staircase model of the disk antenna curvature. The result deviates from the HFSS solution (shown as well for comparison) by ~ 1 dB in the 2 GHz–12 GHz range.

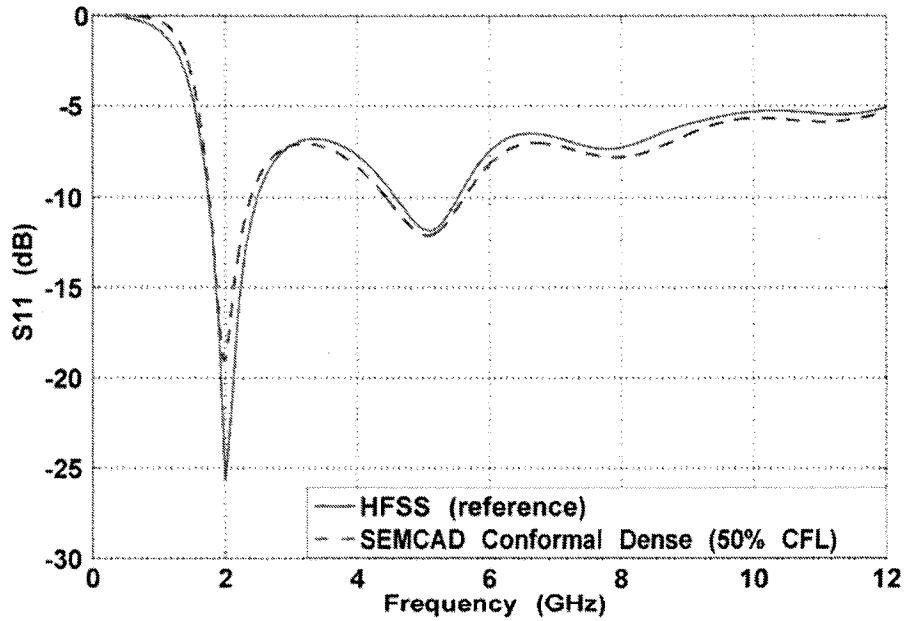


Fig. 5. SEMCAD result for the return loss computed with the dense conformal model of the disk antenna curvature. The result deviates from the HFSS solution (shown as well for comparison) by ~ 0.3 dB in the 2 GHz – 12 GHz range.

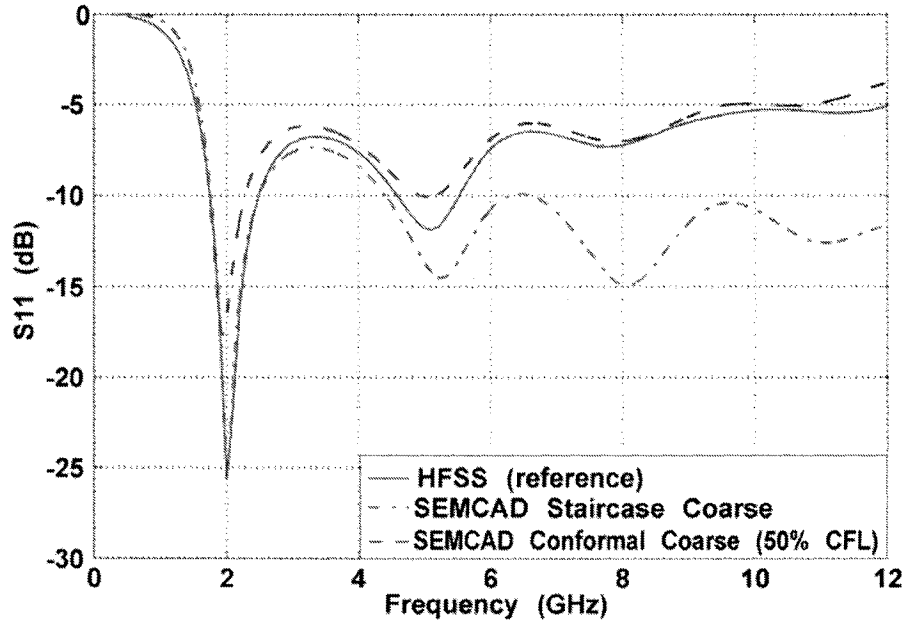


Fig. 6. SEMCAD results for the antenna return loss computed with coarse grid. As can be seen, the coarseness of the grid results in a large degradation of solution accuracy for the staircase model, however, the conformal solver recovers the solution very well with an accuracy of less than ~ 2 dB error over the entire frequency range.

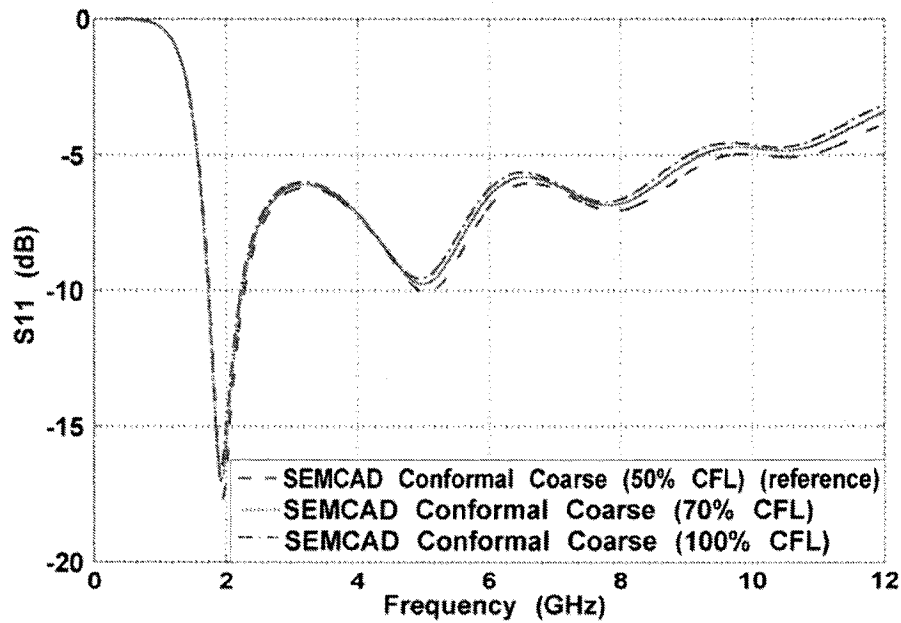


Figure 7. SEMCAD results for the antenna return loss computed with the same coarse grid but with different Courant-Friedrich-Levy (CFL) criterion.

Summary of parameters and the resulting computational resources needed for the SEMCAD models used to assess the accuracy of return loss calculations for antenna of Figure 1. The free space region has the same spatial resolution in all cases (in both x - and y -direction) as follows: maximum step 2 mm while the minimum step is defined by the minimum step size in the antenna region. In antenna region the maximum step size is adjusted to generate dense and coarse grids while the minimum step size in antenna region is computed automatically by SEMCAD as shown in the table. For all regions, in z -direction, the minimum step is set to 0.035 mm and the maximum to 2 mm. The calculations were carried out on a Dell Precision 670, CPU: Dual-Core 2.80 GHz Intel Xeon, Memory: 4 GB DDR2 SDRAM. Average speed and Simulation time are shown for simulations with and without AxFDTD accelerator card [6].

	Max step size in the x - and y -direction in antenna region	Min step size in the x - and y -direction in antenna region	Grid size	Conformal FDTD (50% CFL)		staircase FDTD	
				Average speed (M cell/s)	Simulation time	Average speed (M cell/s)	Simulation time
Dense	0.2 mm	x -dir: 0.2 mm y -dir: 0.2 mm	203x357x69 = ~5 M cells	58.06 / 8.78	1:27:34 / 9:36:00	63.35 / 9.08	0:40:22 / 4:39:18
Coarse	2 mm	x -dir: 1.5 mm y -dir: 1 mm	59x76x69 = ~0.3 M cells	26.89 / 8.44	0:11:14 / 0:35:21	28.55 / 8.61	0:05:20 / 0:17:26

5. Conclusion

In this case study, we examined different FDTD solvers implemented in SEMCAD by comparing the results of the simulated return loss for a disk dipole antenna in the 0.5 GHz –12 GHz range. Our results confirm that, for a structure with curved boundaries, the conformal scheme solution introduces a significant improvement in accuracy when compared with the result from the staircase model of the same FDTD grid density. Further, when the conformal solver is used with a coarse resolution and compared with standard FDTD with a dense FDTD grid, the conformal solution has an excellent accuracy with an order of magnitude reduction in usage of memory and computational time.

Acknowledgement

This work was funded by Natural Science and Engineering Research Council (NSERC) of Canada Discovery Grant and by the Le Fonds Québécois de la recherche sur la Nature et les Technologies Nouveaux Chercheurs Grant. The authors are grateful for help offered by the SEMCAD support staff.

References

- [1] M. Thomas et al, "Wideband Arrayable Planar Radiator", U.S. Patent 5,319,377 (June 7, 1994).
- [2] C. Duncan, "Half disc element dipole antenna", *Antennas and Propagation Society International Symposium, 2005 IEEE*, Vol. 2B, pp. 576- 579, July 2005.
- [3] Ansoft Corporation, information about HFSS is available at <http://www.ansoft.com>.
- [4] Schmidt and Partner Engineering, information about finite-difference time-domain software SEMCAD is available at <http://www.semcad.com/en/tcad/index.php>.
- [5] S. Benkler, N. Chavannes, and N. Kuster, "A New 3-D Conformal PEC FDTD Scheme With User-Defined Geometric Precision and Derived Stability Criterion," *IEEE Trans. Antennas Propagat.*, Vol. 54, pp. 1843-1849, June 2006.
- [6] Acceleware Corporation, information about computational acceleration products is available at <http://www.acceleware.com>

Appendix B

Matlab script used to calculate the magnitude of electric field as a function of z (depth into tissue layers)

```
% Skin(3.7mm) - Fat(20 mm) - Muscle(20mm) model @ 403.5 MH
% -----
% -----
clear;
clc;
Frequency = 403500000;
Omiga = 2*pi*Frequency;

% region 1: Air
RelativeEpsilonAir = 1;
SigmaAir = 0;
RelativeMuAir = 1;
MuAir = RelativeMuAir*4*pi*10^-7;
EpsilonAir = RelativeEpsilonAir*8.8541878176*10^-12;
EpsilonAir1 = EpsilonAir;
EpsilonAir2 = SigmaAir/Omiga;
GamaAir = j*Omiga*sqrt(MuAir*(EpsilonAir1-j*EpsilonAir2));
AlphaAir = real(GamaAir);
BetaAir = imag(GamaAir);
ZAir =sqrt(MuAir/EpsilonAir)/(1+(EpsilonAir2/EpsilonAir1)^2)^0.25
*exp(j/2*atan(EpsilonAir2/EpsilonAir1));

% region 2: Skin
RelativeEpsilonSkin = 48.0603;
SigmaSkin = 0.6811;
RelativeMuSkin = 1;
ThickSkin= 0.0037;
MuSkin = RelativeMuSkin*4*pi*10^-7;
EpsilonSkin = RelativeEpsilonSkin*8.8541878176*10^-12;
EpsilonSkin1 = EpsilonSkin;
EpsilonSkin2 = SigmaSkin/Omiga;
GamaSkin = j*Omiga*sqrt(MuSkin*(EpsilonSkin1-j*EpsilonSkin2));
AlphaSkin = real(GamaSkin);
BetaSkin = imag(GamaSkin);
ZSkin = sqrt(MuSkin/EpsilonSkin)/(1+(EpsilonSkin2/EpsilonSkin1)^2)^0.25*...
exp(j/2*atan(EpsilonSkin2/EpsilonSkin1));

% region 3: Fat
RelativeEpsilonFat = 5.5785;
SigmaFat = 0.041167;
RelativeMuFat = 1;
ThickFat= 0.02;
MuFat = RelativeMuFat*4*pi*10^-7;
EpsilonFat = RelativeEpsilonFat*8.8541878176*10^-12;
```

```

EpsilonFat1 = EpsilonFat;
EpsilonFat2 = SigmaFat/Omiga;
GamaFat = j*Omiga*sqrt(MuFat*(EpsilonFat1-j*EpsilonFat2));
AlphaFat = real(GamaFat);
BetaFat = imag(GamaFat);
ZFat = sqrt(MuFat/EpsilonFat)/(1+(EpsilonFat2/EpsilonFat1)^2)^0.25*...
exp(j/2*atan(EpsilonFat2/EpsilonFat1));

% region 4: Muscle
RelativeEpsilonMuscle = 57.104;
SigmaMuscle = 0.79708;
RelativeMuMuscle = 1;
ThickMuscle= 0.02;
MuMuscle = RelativeMuMuscle*4*pi*10^-7;
EpsilonMuscle = RelativeEpsilonMuscle*8.8541878176*10^-12;
EpsilonMuscle1 = EpsilonMuscle;
EpsilonMuscle2 = SigmaMuscle/Omiga;
GamaMuscle = j*Omiga*sqrt(MuMuscle*(EpsilonMuscle1-j*EpsilonMuscle2));
AlphaMuscle = real(GamaMuscle);
BetaMuscle = imag(GamaMuscle);
ZMuscle
=sqrt(MuMuscle/EpsilonMuscle)/(1+(EpsilonMuscle2/EpsilonMuscle1)^2)^0.25*...
*exp(j/2*atan(EpsilonMuscle2/EpsilonMuscle1));

Coefficient = [1      -1      -1      0      0      0      0
0;...

                1/ZAir 1/ZSkin -1/ZSkin 0      0      0      0
0;...

                0 1*exp(-GamaSkin*ThickSkin) 1*exp(GamaSkin*ThickSkin)...
-1*exp(-GamaFat*ThickSkin) -1*exp(GamaFat*ThickSkin) 0      0
0;...

                0 1/ZSkin*exp(-GamaSkin*ThickSkin)...
-1/ZSkin*exp(GamaSkin*ThickSkin) -1/ZFat*exp(-GamaFat*ThickSkin)
1/ZFat*exp(GamaFat*ThickSkin) 0      0      0;...

                0 0 0      exp(-GamaFat*(ThickSkin+ThickFat))...
exp(GamaFat*(ThickSkin+ThickFat))
-exp(-GamaMuscle*(ThickSkin+ThickFat))...
-exp(GamaMuscle*(ThickSkin+ThickFat))
0;...

                0 0 0      1/ZFat*exp(-GamaFat*(ThickSkin+ThickFat))...
-1/ZFat*exp(GamaFat*(ThickSkin+ThickFat))...
-1/ZMuscle*exp(-GamaMuscle*(ThickSkin+ThickFat))...
1/ZMuscle*exp(GamaMuscle*(ThickSkin+ThickFat))
0;...

                0 0 0      0      0
exp(-GamaMuscle*(ThickSkin+ThickFat+ThickMuscle))...
exp(GamaMuscle*(ThickSkin+ThickFat+ThickMuscle))...
-exp(-GamaAir*(ThickSkin+ThickFat+ThickMuscle));...

```

```

0 0 0 0 0
1/ZMuscle*exp(-GamaMuscle*(ThickSkin+ThickFat+ThickMuscle))...
-1/ZMuscle*exp(GamaMuscle*(ThickSkin+ThickFat+ThickMuscle)) ...
-1/ZAir*exp(-GamaAir*(ThickSkin+ThickFat+ThickMuscle))];

E1p = 1;
E = inv(Coefficient)*[-E1p;E1p/ZAir;0;0;0;0;0;0;0]
E1n = E(1);
E2p = E(2);
E2n = E(3);
E3p = E(4);
E3n = E(5);
E4p = E(6);
E4n = E(7);
E5p = E(8);

for z = 1:100
    d = (z-100)*10/99*0.001;
    E1(z) = E1p*exp(-GamaAir*d)+E1n*exp(GamaAir*d);
end

for z = 101:137
    d = (z-101)*3.7/36*0.001;
    E1(z) = E2p*exp(-GamaSkin*d)+E2n*exp(GamaSkin*d);
end

for z = 138:338
    d = (z-101)*0.1*0.001;
    E1(z) = E3p*exp(-GamaFat*d)+E3n*exp(GamaFat*d);
end

for z = 339:539
    d = (z-102)*0.1*0.001;
    E1(z) = E4p*exp(-GamaMuscle*d)+E4n*exp(GamaMuscle*d);
end

for z = 540:640
    d = (z-103)*0.1*0.001;
    E1(z) = E5p*exp(-GamaAir*d);
end

plot ([-10:0.1:53.9], abs(E1),'r');
% Skin(3.7mm) - Fat(20 mm) - Muscle(20mm) model @ 403.5 MH end
% -----
% -----

```

Appendix C

Matlab script used to convert Cole-Cole model to Debye model for SEMCAD-X by Minimum Square Error curve fitting

```

% Fat
% pole = [0.2*10^9 12*10^9 50*10^9]*2*pi;
clear;
clc;
load ('D:\YI\McGill\Thesis\parameter study\Fat.txt');
Sigma = 0.01;
ColeEpsilonInf = 2.5;
DebyeEpsilonInf = ColeEpsilonInf;
ColeEpsilonS = [3 15 3.3*10^4 1.0*10^7]+'ColeEpsilonInf;
DebyeEpsilonS = ColeEpsilonS(1);
ColeTao = [7.96*10^-12 15.92*10^-9 159.15*10^-6 7.958*10^-3]';
ColeAlpha = [0.2 0.1 0.05 0.01]';

pole = [0.2*10^9 12*10^9 50*10^9]*2*pi;
relaxationTime = 1./pole

% ColeCole Calculation
for freq = 10^9:10^9:10^11
    Temp = ColeEpsilonInf +
    sum((ColeEpsilonS-ColeEpsilonInf)./(1+(j*2*pi*freq*ColeTao).^ (1-ColeAlpha))
    )+Sigma/(j*2*pi*freq*8.8541878176*10^-12);
    EpsilonCole (freq/10^9,:) = [real(Temp),-imag(Temp)];
end

frequency = [10^9: 10^9: 10^11]';
omega = frequency*2*pi;

c = EpsilonCole(:,2)/(ColeEpsilonS(1)-ColeEpsilonInf);

for index = 1:100
    for jindex = 1:3
        D(index,jindex) =
    omega(index)/pole(jindex)/(1+(omega(index)/pole(jindex))^2);
    end
end

a = inv(D'*D)*D'*c;

temp = 0;
for index = 1:100
    temp = temp +
    EpsilonCole(index,1)-ColeEpsilonInf-(DebyeEpsilonS-DebyeEpsilonInf)*sum(a./
    (1+(omega(index)./pole).^2));
end

```

```

average = temp/100;

% Verfication of the Debye model
for freq = 10^9:10^9:10^11
    Temp =
DebyeEpsilonInf+(DebyeEpsilonS-DebyeEpsilonInf)*sum(a./(1+j*2*pi*freq./pole
))+average;
    EpsilonDebye (freq/10^9,:) =
[real(Temp),-imag(Temp)*2*pi*freq*8.8541878176*10^-12];
end

semilogx (Fat(:,1),Fat(:,3),'.',Fat(:,1),Fat(:,2),'.')
hold on;
semilogx (frequency,EpsilonDebye(:,1),':',frequency,EpsilonDebye(:,2),':')
semilogx
(frequency,EpsilonCole(:,1),frequency,EpsilonCole(:,2).*frequency*2*pi*8.85
41878176*10^-12,'r')
legend ('Tabled Permittivity','Tabled Conductivity', 'Debye
Permittivity','Debye Conductivity','Cole-Cole Permittivity','Cole-Cole
Conductivity')

```